Finite Element Discretization of a Stokes-like Model Arising in Plasma Physics

Juan Vicente Gutiérrez Santacreu[a], Omar Maj[b], and Marco Restelli*[b]

[a] *Dpto. de Matemática Aplicada I, Universidad de Sevilla, E. T. S. I. Informática. Avda. Reina Mercedes s/n, 41012 Sevilla, Spain.*

[b] *Numerische Methoden in der Plasmaphysik, Max-Planck-Institut für Plasmaphysik. Boltzmannstr. 2, 85748 Garching, Germany.*

Abstract

We consider a time-dependent diffusion-reaction model for two vector unknowns, satisfying a divergence-free constraint, and the associated scalar Lagrange multiplier. The motivation for studying such a model is provided by a plasma physics problem arising in the modeling of nuclear fusion devices (Braginskii equations), where the two vector unknowns represent ion and electron velocities, the scalar unknown is the electrostatic potential and the divergence-free constraint reflects the physical assumption of quasi-neutrality. We first recast the problem in a form reminiscent of the standard Stokes problem, which allows us to recognize the importance of using a compatible discretization for the vector and scalar unknowns, then propose and analyze a stable finite element formulation. Following this, we address some peculiar geometrical aspects of the model, showing how they can be naturally dealt with within our formulation, and finally discuss a solution procedure for the resulting linear system based on the classical Uzawa algorithm. Some numerical experiments complete the paper.

Keywords. Finite elements inf-sup stable discretization Braginskii equations quasi-neutrality condition plasma physics tokamak modeling MCS[2010] 65M60 76D07 76M10 76W05 76X05 82D10

1 Introduction

The magnetic confinement approach to nuclear fusion for civil applications relies on the construction of large toroidal devices where a hydrogen plasma is heated while being confined by a strong magnetic field. In order to obtain the plasma ignition, three simultaneous conditions must be fulfilled: high temperature, high density and long confinement time. Ensuring these conditions has proven to be a major technological challenge, which must be supported by a deep physical understanding of the involved processes; in this context, an important role is played by the use of numerical models.

*Corresponding author `marco.restelli@ipp.mpg.de`

In this paper, we are interested in fluid models which are used to describe the heat and particle fluxes occurring in the peripheral region of the confined plasma, the so-called Scrape-off Layer (SOL) [1]. A suitable model for the SOL is the following fluid system (see (2.1e)–(2.3i) in [2, § 2])

$$\partial_t n_\alpha + \nabla \cdot (n_\alpha \boldsymbol{u}_\alpha) = S_{n,\alpha}, \tag{1}$$

$$\begin{aligned}\partial_t \left(m_\alpha n_\alpha \boldsymbol{u}_\alpha\right) &+ \nabla \cdot \left(m_\alpha n_\alpha \boldsymbol{u}_\alpha \otimes \boldsymbol{u}_\alpha + \boldsymbol{\pi}_\alpha\right) \\ &= -\nabla p_\alpha + e_\alpha n_\alpha \left(-\nabla \Phi + \tfrac{1}{c} \boldsymbol{u}_\alpha \times \boldsymbol{B}\right) + \boldsymbol{R}_\alpha + \boldsymbol{S}_{M,\alpha},\end{aligned} \tag{2}$$

$$\partial_t \left(\tfrac{3}{2} p_\alpha\right) + \nabla \cdot \left(\tfrac{3}{2} p_\alpha \boldsymbol{u}_\alpha + \boldsymbol{q}_\alpha\right) + p_\alpha \nabla \cdot \boldsymbol{u}_\alpha + \boldsymbol{\pi}_\alpha : \nabla \boldsymbol{u}_\alpha = Q_\alpha + S_{T,\alpha}, \tag{3}$$

$$\nabla \cdot \boldsymbol{J} = 0. \tag{4}$$

Here, α denotes the various ion species as well as the electrons, characterized by their mass m_α, charge e_α, number density n_α, velocity $\boldsymbol{u}_\alpha$ and pressure p_α; Φ and $\boldsymbol{B}$ denote the electrostatic potential and the magnetic field, respectively, c is the speed of light, $\boldsymbol{\pi}_\alpha$ and $\boldsymbol{q}_\alpha$ are momentum and energy fluxes, $\boldsymbol{R}_\alpha$ and Q_α represent the momentum and energy exchanges among the various species, and $S_{n,\alpha}, \boldsymbol{S}_{M,\alpha}, S_{T,\alpha}$ are particle, momentum and energy sources, respectively. Finally, $\boldsymbol{J}$ is the current resulting from the plasma flow, defined by

$$\boldsymbol{J} = \sum_\alpha e_\alpha n_\alpha \boldsymbol{u}_\alpha.$$

Constitutive equations for $\boldsymbol{\pi}_\alpha$, $\boldsymbol{q}_\alpha$, $\boldsymbol{R}_\alpha$ and Q_α are derived in [2] from the kinetic description of the system, the source terms are assumed to be prescribed and the magnetic field is assumed to be known and constant, thereby assuming that the equilibrium field, produced by external coils and by the plasma current, is much larger than the changes in $\boldsymbol{B}$ caused by the transport processes; under such assumptions, and provided that suitable initial and boundary conditions have been specified, system (1)–(4) represents a closed initial-boundary value problem.

Equation (4) is referred to as *quasi-neutrality condition*, since it prevents the local build-up of electric charge. For a plasma, net electric charge appears on spatial scales comparable with the Debye length, which is much smaller than the size of technical devices, so that quasi-neutrality is a correct assumption. Such an assumption has a fundamental impact on the fluid model, for which an interesting parallel can be drawn with the incompressibility assumption in standard fluid mechanics; this is one of the main focuses of the present paper and will be discussed in further details in the following.

For typical fusion devices, the Lorentz force terms proportional to $\nabla\Phi$ and $\boldsymbol{u}_\alpha \times \boldsymbol{B}$ are by far the dominating ones in the momentum equation (2), together with the pressure gradient terms, so that the geometry of $\boldsymbol{B}$, and in particular the topology of its flux surfaces, are of paramount importance in the study of (1)–(4). Given the complexity of the magnetic geometry in technical devices (see for instance [3]), its accurate representation is a challenge for any numerical method, and has motivated many authors to explore various approaches concerning the numerical discretization and the choice of the computational grid.

A class of models based on an approximation of (1)–(4) known as *drift-reduced equations* [4, 5], aiming at extracting the dominant physical processes, isolating some stiff terms, and mitigating the computational cost, is used in various codes for the simulation of the SOL, either in the transport or the turbulent regime, such as [6, 7, 8, 9, 10, 11, 12, 13, 14, 15, 16, 17]. Despite the large variety of the proposed drift-reduced models, common aspects of such models are: a) projecting the momentum equation (2) in the directions parallel and perpendicular to $\boldsymbol{B}$; b) using the resulting perpendicular

momentum equation to obtain, upon discarding some small terms, an algebraic expression for the perpendicular velocity (the "drifts"), which is then substituted at the continuous level in the remaining equations; c) substituting n_α and $\boldsymbol{u}_\alpha$ into (4) to obtain an elliptic equation for Φ, again at the continuous level, and finally d) discretizing the resulting system.

Concerning the numerical discretization, the importance of a flexible strategy in the construction of the computational grid has been recognized in many publications. A first requirement, as pointed out in [10], is that, due to the strong anisotropy of the problem in the directions parallel and perpendicular to $\boldsymbol{B}$, "[...] it is essential that the mesh be aligned with the flux surfaces; i.e. for most triangles, there should be one side with its two extremities lying on the same flux surface." Another important aspect is allowing for local refinement in regions with sharp gradients and regions which are particularly critical for the correct computation of the source terms, such as the divertor plates. Finally, it is desirable to extend the grid until the wall of the confinement vessel, which typically has an irregular geometry. The proposed approaches include block structured grids with cut cells [18], fully unstructured triangular grids [19, 20, 10, 21, 22, 23, 24], and hybrid grids combining both structured and unstructured blocks [25, 26].

As an alternative to the drift-reduced approach, one could consider solving directly (1)–(4), taking advantage of the increase in available computational power with respect to the time when the first drift-reduced models were introduced. In fact, this would be appealing for at least two reasons: on the one hand, the structure of (1)–(4) is the same encountered in compressible fluid dynamics problems, as opposite to the Poisson bracket nonlinearity appearing in the drift-reduced system, which would allow us to use more standard and well established techniques; on the other hand, such a system offers the possibility to treat the electric potential Φ as the Lagrange multiplier associated with the quasi-neutrality condition, as it will be discussed in the rest of the present paper, thereby providing a solid ground for its treatment from both the continuous and the discrete viewpoint.

As a first step towards exploring the feasibility of discretizing directly (1)–(4), we consider here an extremely stripped-down version of the problem, retaining the following ingredients: the velocities $\boldsymbol{u}$ and $\boldsymbol{u}_\mathrm{e}$ of one ion species and of the electrons, respectively, the corresponding Lorentz force terms $-\nabla\Phi + \boldsymbol{u}\times\boldsymbol{B}$ and $\nabla\Phi - \boldsymbol{u}_\mathrm{e}\times\boldsymbol{B}$, and the quasi-neutrality condition. We stress the fact that this model is not a consistent asymptotic version of (1)–(4), instead, those terms are retained which model the quasi-neutral limit and the magnetic geometry. The resulting system is

$$\partial_t \boldsymbol{u} = -\nabla\Phi + \boldsymbol{u}\times\boldsymbol{B} + \nu\Delta\boldsymbol{u} + \boldsymbol{f}, \tag{5}$$

$$0 = \quad \nabla\Phi - \boldsymbol{u}_\mathrm{e}\times\boldsymbol{B} + \nu_\mathrm{e}\Delta\boldsymbol{u}_\mathrm{e} + \boldsymbol{f}_\mathrm{e}, \tag{6}$$

$$\nabla\cdot(\boldsymbol{u} - \boldsymbol{u}_\mathrm{e}) = 0, \tag{7}$$

complemented with Dirichlet boundary conditions for $\boldsymbol{u}$ and $\boldsymbol{u}_\mathrm{e}$, either homogeneous, to simplify the analysis, or inhomogeneous, in the numerical tests. Notice that in (5)–(7) the electron mass has been neglected, which is an assumption also adopted in the drift-reduced models, and the dissipative effects have been represented by simple diffusive terms with prescribed, constant coefficients ν, ν_e. The use of Dirichlet boundary conditions for the ion and electron velocities is motivated by the fact that this ensures the well-posedness of the problem, as will be clear from the rest of the paper. Physically correct boundary conditions would include nonlinear terms to model the plasma sheets, microscopic layers where (1)–(4) break down [1, 26]); numerical modeling of the plasma sheets however constitutes an actual research topic on its own and is outside the scope of the present analysis. Concerning the computational domain, we focus on transport processes and consider an axisymmetric problem, so that, in a cylindrical coordinate system R, z, φ, each quantity is a function

of two spatial variables R, z; despite this reduction to a two-dimensional computational domain, however, we retain the three-dimensional character of the velocity vectors $\boldsymbol{u}, \boldsymbol{u}_\mathrm{e}$ as well as of the magnetic field $\boldsymbol{B}$, in order to represent the effects associated with the nontrivial geometry of the problem.

The goal of this paper is addressing the following aspects: mathematical well-posedness of (5)–(7), definition of a suitable finite element discretization for such a problem, definition of an efficient solution procedure for the computation of the electric potential Φ, and providing a correct framework for the treatment of the three-dimensional geometrical aspects. The well-posedness derives from a stability argument for Φ, regarded as Lagrange multiplier; a stable finite element formulation can then be derived using classical finite element spaces for the Stokes problem. The computation of Φ can be performed adapting the Uzawa algorithm, taking into account that, due to the Lorentz force, the operator is not self-adjoint. Finally, to handle the geometrical complexity we introduce three ingredients: the problem is treated in three spatial dimensions, introducing the axial symmetry through the finite element space; a hybrid, unstructured mesh composed both of triangles and quadrilaterals is adopted; a nonstandard representation for the discrete velocity is introduced.

The rest of the paper is organized as follows: § 2 discusses some qualitative aspects of (5)–(7), relating them to the full system (1)–(4) as well as to the drift-reduced models; § 3 summarizes the geometry of the problem; § 4 and § 5 are devoted to the well-posedness of the continuous and discrete formulations, respectively; § 6 addresses various issues which are crucial for an efficient and accurate computational strategy; finally, § 7 presents a numerical verification of the proposed method. § 8 draws some conclusions and provides some outlooks.

2 Qualitative aspects of the model

As already mentioned, the Lorentz force terms are the dominant ones in (5) and (6), so that the solution of (5)–(7) is characterized by

$$\boldsymbol{u}^\perp \approx \boldsymbol{u}_\mathrm{e}^\perp \approx \frac{-\nabla\Phi \times \boldsymbol{B}}{B^2}, \qquad (\nabla\Phi)^\parallel \approx 0, \tag{8}$$

where the superscripts $\parallel$ and $\perp$ denote the parallel and perpendicular directions to $\boldsymbol{B}$, respectively (see also § 3 for additional details). This qualitative behavior is also relevant for the complete problem (1)–(4) and defines one of the fundamental drifts accounted for in the drift-reduced models, namely the *E cross B* drift $\boldsymbol{u}_E = \frac{-\nabla\Phi\times\boldsymbol{B}}{B^2}$. The main problem with (8) is that nothing can be concluded about the electrostatic potential Φ, and more precisely about its variation in the directions perpendicular to $\boldsymbol{B}$. In fact, since (8) yields equal velocities for ions and electrons, condition (7) is trivially satisfied for any choice of Φ. Hence, terms other than the Lorentz force in (5)–(7), despite being smaller than the latter, have a fundamental importance in shaping the electrostatic potential and, by virtue of (8), the ion velocities. Such terms are the ion inertia $\partial_t \boldsymbol{u}$ and the momentum dissipative fluxes $\nu\Delta\boldsymbol{u}$ and $\nu_\mathrm{e}\Delta\boldsymbol{u}_\mathrm{e}$, which appear in our reduced model as proxies of the material derivative of the ion momentum and of the friction terms of the complete model (1)–(4), respectively.

In the terminology of the drift-reduced models, the $\boldsymbol{u}_E$ drift is said to be *ambipolar*, meaning that it does not differentiate between positive and negative charged particles, while other terms in (5)–(7) which differentiate between ions and electrons are collectively referred to as *polarization current*.

The computation of Φ taking into account the polarization current is a delicate component of the drift-reduced models. A typical approach consists in separating this computation in two steps: along the parallel and the perpendicular directions to $\boldsymbol{B}$. In the parallel direction, i.e. along the magnetic field lines, the condition $(\nabla\Phi)^{\parallel} = 0$, from (8), can be used (or, more precisely, its correspondent form derived projecting the electron momentum equation in (2) in the parallel direction). For open field lines, i.e. for magnetic field lines which intersect the boundary of the domain, this can be used to "propagate" a boundary condition for Φ inside the domain, thereby fully determining the electrostatic potential. For closed field lines on the contrary, i.e. for magnetic field lines which close upon themselves inside the domain without intersecting the boundary, prescribing $(\nabla\Phi)^{\parallel}$ is not enough and $(\nabla\Phi)^{\perp}$ must be taken into account. A possible approach is performing some algebraic manipulations on (1)–(4) in order to isolate an elliptic problem for Φ of the form (omitting some terms which are not relevant for the point being discussed)

$$\nabla \cdot \left(\sigma_{\parallel} (\nabla\Phi)^{\parallel} + \sigma_{\mathrm{an}} (\nabla\Phi)^{\perp} \right) = \mathrm{rhs}. \tag{9}$$

However, while $\sigma_{\parallel}$ and the right-hand side of (9) are derived directly from the complete problem (1)–(4), σ_{an} is "an ad hoc anomalous perpendicular conductivity" (see [10, § 2.7]), and hence the term involving the perpendicular derivatives of Φ is not consistent with the complete Braginskii equations. Such an approach is used in the SOLPS family of models [8, 9, 11, 12], which are used to simulate the SOL in axisymmetric devices for long time scales and thus represent a direct reference for our work. As observed in [11, § 3], despite the possibility to justify, in principle, the introduction of σ_{an} by means of physical arguments, in practice this parameter is treated as a tuning parameter to ensure convergence of the numerical scheme and can have a significant impact on the computed solution.

In this paper we explore an alternative approach which does not rely on the introduction of any anomalous perpendicular conductivity but rather computes Φ by regarding it in (5) and (6) as the Lagrange multiplier associated with the (charge) incompressibility condition (7), and then resorting to standard techniques for the incompressible Stokes problem.

We emphasize that the analogy between the quasi-neutrality condition and the incompressible fluid dynamics is not due to a simple formal correspondence of our reduced model (5)–(7) with the Stokes system; rather, there is a deep physical correspondence between the quasi-neutrality assumption in the Braginskii system (1)–(4) and the motivation for considering nondivergent flows in standard fluid dynamics. In fact, in fluid dynamics a divergent mass flow results in density variations, which cause pressure fluctuations through the equation of state, which ultimately tend to counteract the density variations themselves. Whenever the dynamics of these fluctuations is much faster than the time scale of the problem being considered (i.e. for low Mach numbers) it is justified, and computationally convenient, to eliminate them altogether enforcing a divergent free mass flow. Having eliminated the density variations from the system, the pressure fluctuations are not determined anymore by the equation of state, but instead take the role of Lagrange multiplier ensuring the fulfillment of the zero divergent constraint. For a plasma, a current with nonvanishing divergence results in local charge build-up, which causes electric potential fluctuations through the Maxwell equations, which ultimately tend to restore an electrically neutral condition. Since the dynamics of these electric oscillations is much faster than the time scales considered in the SOL modeling, it is justified to eliminate the charge fluctuations enforcing a nondivergent current. This however prevents us from using the Maxwell equations to compute Φ, which instead can be determined as the Lagrange multiplier ensuring local quasi-neutrality. This is outlined in Table 1.

For a more rigorous treatment of the quasi-neutral limit, the interested reader can consider [27, 28].

compressible fluid dynamics	incompressible fluid dynamics
prognostic continuity equation for ρ state equation: $p = p(\rho)$ sound waves	time independent constraint $\nabla \cdot \boldsymbol{u} = 0$ p Lagrange multiplier for $\nabla \cdot \boldsymbol{u} = 0$
plasma, local charge build-up	plasma, quasi-neutrality
prognostic equation for $\rho_c = \sum_\alpha e_\alpha n_\alpha$ Maxwell equation: $\Phi = \Phi(\rho_c)$ plasma frequency	time independent constraint $\nabla \cdot \boldsymbol{J} = 0$ Φ Lagrange multiplier for $\nabla \cdot \boldsymbol{J} = 0$

Table 1: Schematic comparison of the assumptions of incompressibility and quasi-neutrality in fluid mechanics and plasma physics, respectively. Notice the correspondence between the mass and charge densities, ρ and ρ_c, as well as between the pressure p and the electrostatic potential Φ.

3 Problem geometry

To simulate technical devices, the governing equations for the plasma flow must be solved in the three-dimensional region occupied by the plasma itself. Hence, (5)–(7) must be considered within a bounded domain $\Omega \subset \mathbb{R}^3$ and $\boldsymbol{u}$, $\boldsymbol{u}_\mathrm{e}$, $\boldsymbol{B}$, as well as the forcing terms, are vector fields taking values in $\mathbb{R}^3$. At the same time, given that an important class of fusion devices, the so-called *tokamaks*, is characterized by axial symmetry, and given that in many cases an axially averaged computation, which neglects the symmetry breaking fluctuations of the flow, can be considered satisfactory, two-dimensional simulations in the $R-z$ plane are also of great interest (this is indeed the case considered in the SOLPS code suite). This motivates us to consider both two and three-dimensional versions of (5)–(7).

A convenient way to handle both formulations is working with the weak form of the problem, deriving the axially symmetric case from the general three-dimensional one. Assuming homogeneous boundary conditions

$$\boldsymbol{u} = \boldsymbol{u}_\mathrm{e} = 0 \ \text{ on } \ \partial\Omega,$$

the three-dimensional weak form of (5)–(7) is readily obtained multiplying each equation by a test function, formally integrating over Ω, integrating by parts and using the boundary conditions for $\boldsymbol{u}_\mathrm{e}$ and $\boldsymbol{u}$, arriving at

$$\int_\Omega [\partial_t \boldsymbol{u} \cdot \boldsymbol{v} + \nu \nabla \boldsymbol{u} : \nabla \boldsymbol{v} - \Phi \nabla \cdot \boldsymbol{v} - \boldsymbol{u} \times \boldsymbol{B} \cdot \boldsymbol{v}] \, \mathrm{d}\boldsymbol{x} = \int_\Omega \boldsymbol{f} \cdot \boldsymbol{v} \, \mathrm{d}\boldsymbol{x}, \tag{10}$$

$$\int_\Omega [\nu_\mathrm{e} \nabla \boldsymbol{u}_\mathrm{e} : \nabla \boldsymbol{v}_\mathrm{e} + \Phi \nabla \cdot \boldsymbol{v}_\mathrm{e} + \boldsymbol{u}_\mathrm{e} \times \boldsymbol{B} \cdot \boldsymbol{v}_\mathrm{e}] \, \mathrm{d}\boldsymbol{x} = \int_\Omega \boldsymbol{f}_\mathrm{e} \cdot \boldsymbol{v}_\mathrm{e} \, \mathrm{d}\boldsymbol{x}, \tag{11}$$

$$\int_\Omega \nabla \cdot (\boldsymbol{u} - \boldsymbol{u}_\mathrm{e}) q \, \mathrm{d}\boldsymbol{x} = 0. \tag{12}$$

To obtain the axially averaged problem, we need to outline the design of a tokamak device, as illustrated in Figures 1 and 2 (see also [1]). Let us first introduce cylindrical coordinates R, z, φ.

For an axially symmetric system, the cylindrical angle φ is the homogeneity variable, i.e. nothing in the system depends on such a variable. The magnetic field $\boldsymbol{B}$ winds around the circle $R = R_0, z = 0$, which is the *magnetic axis*, denoted by μ, and around the major axis z, thus defining field lines and magnetic surfaces. Inner magnetic surfaces are closed and covered by either a single field lines or, for *rational surfaces*, by a collection of field lines, while outer magnetic surfaces intercept the boundary of the domain; closed and open magnetic surfaces are separated by the *last closed magnetic surface*. Half planes $R \geq 0$, $\varphi = Const$ are called poloidal planes. Due to the toroidal

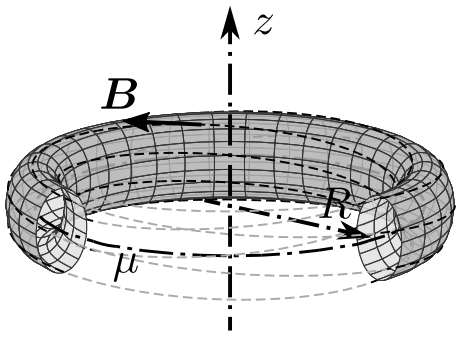

Figure 1: Outline of the design the a tokamak device. The magnetic field $\boldsymbol{B}$ winds around the magnetic axis μ and the major axis z. This plot shows a closed magnetic surface, i.e. a closed surface covered by a single magnetic line.

symmetry of the device, the three-dimensional domain Ω can be represented as $\Omega = \tilde{\Omega} \times [-\pi, \pi)$, where $\tilde{\Omega}$ is the poloidal section $\Omega \cap \pi_{\text{pol}}$ and π_{pol} is the poloidal plane $\varphi = 0$. The intersection of the last closed magnetic surface with π_{pol} is the *separatrix*; moreover, on π_{pol}, the *O point* and the *X point* are defined by the intersection with the magnetic axis and the self-intersection of the separatrix, respectively. The separatrix also defines three regions: the main plasma, the scrape-off layer and the private region, as depicted in Figure 2, right. The magnetic field identifies the parallel direction $\boldsymbol{b} = \boldsymbol{B}/B$. Notice that in general $\boldsymbol{b}$ is not perpendicular to the poloidal plane, except at special points such as the O point and the X point. The two-dimensional, toroidally averaged version of (10)–(12) is obtained by considering both test and trial functions to be independent from the homogeneity coordinate φ. This leads to

$$\int_{\tilde{\Omega}} \left[\partial_t \tilde{\boldsymbol{u}} \cdot \tilde{\boldsymbol{v}} + \nu \nabla \tilde{\boldsymbol{u}} : \nabla \tilde{\boldsymbol{v}} - \tilde{\Phi} \nabla \cdot \tilde{\boldsymbol{v}} - \tilde{\boldsymbol{u}} \times \boldsymbol{B} \cdot \tilde{\boldsymbol{v}} \right] R \mathrm{d}\tilde{\boldsymbol{x}} = \int_{\tilde{\Omega}} \boldsymbol{f} \cdot \tilde{\boldsymbol{v}} \, R \mathrm{d}\tilde{\boldsymbol{x}}, \tag{13}$$

$$\int_{\tilde{\Omega}} \left[\nu_{\mathrm{e}} \nabla \tilde{\boldsymbol{u}}_{\mathrm{e}} : \nabla \tilde{\boldsymbol{v}}_{\mathrm{e}} + \tilde{\Phi} \nabla \cdot \tilde{\boldsymbol{v}}_{\mathrm{e}} + \tilde{\boldsymbol{u}}_{\mathrm{e}} \times \boldsymbol{B} \cdot \tilde{\boldsymbol{v}}_{\mathrm{e}} \right] R \mathrm{d}\tilde{\boldsymbol{x}} = \int_{\tilde{\Omega}} \boldsymbol{f}_{\mathrm{e}} \cdot \tilde{\boldsymbol{v}}_{\mathrm{e}} \, R \mathrm{d}\tilde{\boldsymbol{x}}, \tag{14}$$

$$\int_{\tilde{\Omega}} \nabla \cdot (\tilde{\boldsymbol{u}} - \tilde{\boldsymbol{u}}_{\mathrm{e}}) \tilde{q} \, R \mathrm{d}\tilde{\boldsymbol{x}} = 0, \tag{15}$$

with $\mathrm{d}\tilde{\boldsymbol{x}} = \mathrm{d}R\,\mathrm{d}z$. Functions denoted by a tilde can be regarded either as functions of the two variables R, z (and possibly time), defined on $\tilde{\Omega}$, or as functions of R, z, φ defined on Ω and constant in φ. Despite the reduction to a two-dimensional problem, the vector fields in (13)–(15) retain their three-dimensional character, so that $\tilde{\boldsymbol{u}}, \tilde{\boldsymbol{u}}_{\mathrm{e}}$ and $\tilde{\boldsymbol{v}}, \tilde{\boldsymbol{v}}_{\mathrm{e}}$ take values in $\mathbb{R}^3$; the differential operators,

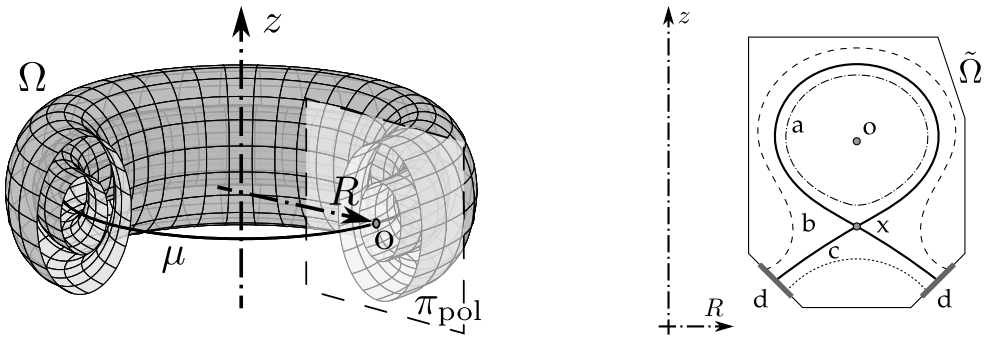

Figure 2: Outline of the design of a tokamak device. Left: three-dimensional view showing two closed magnetic surfaces, the magnetic axis μ, the cylindrical coordinates R, z, one poloidal plane π_{pol} and the O point, i.e. the intersection of the magnetic axis with the poloidal plane. Right: view of the poloidal plane showing the O point and the X point, one closed magnetic surface (dash-dot line), the separatrix (continuous line), two open field lines (dashed line and dotted line) and the two divertor plates d. The right plot shows also the main plasma regions: the main plasma a, the scrape-off layer b and the private region c.

expressed with respect to the coordinate unit vectors $\boldsymbol{e}_R, \boldsymbol{e}_z, \boldsymbol{e}_{-\varphi}$ (where $\boldsymbol{e}_{-\varphi} = -\boldsymbol{e}_\varphi$, the signs being chosen so that the resulting base is right-handed) are

$$\nabla\tilde{\boldsymbol{v}} = \begin{bmatrix} \partial_R\tilde{v}_R & \partial_z\tilde{v}_R & -R^{-1}\tilde{v}_{-\varphi} \\ \partial_R\tilde{v}_z & \partial_z\tilde{v}_z & 0 \\ \partial_R\tilde{v}_{-\varphi} & \partial_z\tilde{v}_{-\varphi} & R^{-1}\tilde{v}_R \end{bmatrix}, \qquad \nabla\cdot\tilde{\boldsymbol{v}} = \partial_R\tilde{v}_R + \partial_z\tilde{v}_z + R^{-1}\tilde{v}_R.$$

We notice that the weak form (13)–(15), combined with the vector notation, allows us to write the axisymmetric problem in a much simpler form compared to the strong, component form used, for instance, in [11]. Finally, we mention that, for all practical applications, R is strictly larger than zero in $\tilde{\Omega}$, i.e. the plasma does not reach the major axis of the device.

4 Analysis of the continuous model

In this section, we consider the well-posedness of the reduced model (5)–(7) in three space dimensions with homogeneous Dirichlet boundary conditions for the ion and electron velocities, without assuming any symmetry of the system. Nevertheless, our analysis readily extends to the axisymmetric case (13)–(15) using the fact that, thanks to $R \geq R_{\min} > 0$,

$$(\tilde{p}, \tilde{q})_\sim = \int_{\tilde{\Omega}} \tilde{p}\tilde{q}\, R\mathrm{d}\tilde{\boldsymbol{x}}$$

defines an equivalent scalar product in $L^2(\tilde{\Omega})$. Hence, let Ω denote a bounded domain in $\mathbb{R}^3$ with Lipschitz continuous boundary $\partial\Omega$, and let $L^p(\Omega)$, for either $p = 2$ or $p = \infty$, and $H^k(\Omega)$, for $k = 1, 2$, denote the standard Lebesgue and Sobolev spaces on Ω. We will also need the subset $H_0^1(\Omega) \subset$

$H^1(\Omega)$ of the functions with vanishing trace on $\partial\Omega$, its dual space $H^{-1}(\Omega) = (H^1_0(\Omega))'$, the subspace $L^2_{\int=0}(\Omega) \subset L^2(\Omega)$ of functions with vanishing mean value and $H^1_{\int=0}(\Omega) = H^1(\Omega) \cap L^2_{\int=0}(\Omega)$; both $H^1_0(\Omega)$ and $H^1_{\int=0}(\Omega)$ are endowed with the norm $\|\nabla q\|_{L^2(\Omega)}$ for a generic function q. The corresponding vector spaces $(H^1_0(\Omega))^d$, $(L^2(\Omega))^d$ and $(H^{-1}(\Omega))^d$ are denoted by $\boldsymbol{H}^1_0(\Omega)$, $\boldsymbol{L}^2(\Omega)$ and $\boldsymbol{H}^{-1}(\Omega)$, respectively. Finally, we introduce the Bochner function spaces $L^p(0,T;X)$ and $L^p(0,T;\boldsymbol{X})$, for $p = 2$ or $p = \infty$, where $(0,T]$ is the time interval and $X, \boldsymbol{X}$ stand for any of scalar or vector function spaces introduced above. In the following, the domain Ω will be omitted whenever there is no ambiguity.

Let $\boldsymbol{B} \in \boldsymbol{L}^\infty$, $\boldsymbol{f}, \boldsymbol{f}_{\mathrm{e}} \in L^2(0,T;\boldsymbol{H}^{-1})$ and $\boldsymbol{u}_0 \in \boldsymbol{L}^2$. The variational formulation of (5)–(7) reads: find $\boldsymbol{u} \in L^2(0,T;\boldsymbol{H}^1_0)$ with $\boldsymbol{u}' \in L^2(0,T;\boldsymbol{H}^{-1})$ (which also implies $\boldsymbol{u} \in C^0(0,T;\boldsymbol{L}^2)$), $\boldsymbol{u}_{\mathrm{e}} \in L^2(0,T;\boldsymbol{H}^1_0)$ and $\Phi \in L^2(0,T,L^2_{\int=0})$ such that, for a. e. $t \in (0,T]$,

$$\langle \boldsymbol{u}', \boldsymbol{v}\rangle + \nu(\nabla \boldsymbol{u}, \nabla \boldsymbol{v}) - (\Phi, \nabla\cdot \boldsymbol{v}) - (\boldsymbol{u}\times\boldsymbol{B}, \boldsymbol{v}) = \langle \boldsymbol{f}, \boldsymbol{v}\rangle\,, \tag{16}$$

$$\nu_{\mathrm{e}}(\nabla \boldsymbol{u}_{\mathrm{e}}, \nabla \boldsymbol{v}_{\mathrm{e}}) + (\Phi, \nabla\cdot \boldsymbol{v}_{\mathrm{e}}) + (\boldsymbol{u}_{\mathrm{e}}\times\boldsymbol{B}, \boldsymbol{v}_{\mathrm{e}}) = \langle \boldsymbol{f}_{\mathrm{e}}, \boldsymbol{v}_{\mathrm{e}}\rangle\,, \tag{17}$$

$$(\nabla\cdot(\boldsymbol{u}-\boldsymbol{u}_{\mathrm{e}}), q) = 0, \tag{18}$$

for all $(\boldsymbol{v}, \boldsymbol{v}_{\mathrm{e}}, q) \in \boldsymbol{H}^1_0 \times \boldsymbol{H}^1_0 \times L^2_{\int=0}$, with

$$\boldsymbol{u}(t=0) = \boldsymbol{u}_0.$$

Well-posedness of this weak formulation is ensured by the following result.

Theorem 1. *Let $\boldsymbol{B}$, $\boldsymbol{f}$, $\boldsymbol{f}_{\mathrm{e}}$ and $\boldsymbol{u}_0$ be as above. Then there exists a unique weak solution $(\boldsymbol{u}, \boldsymbol{u}_{\mathrm{e}}, \Phi)$ of (16)–(18) on $[0,T]$.*

Proof. Since $\boldsymbol{H}^1_0$ and $H^1_{\int=0}$ are separable, there exist two dense sequences $\{\bar{\boldsymbol{v}}_i\}$, $\{\bar{q}_i\}$; let $\boldsymbol{V}_n = \mathrm{span}\{\bar{\boldsymbol{v}}_1, \cdots, \bar{\boldsymbol{v}}_n\}$ and $Q_n = \mathrm{span}\{\bar{q}_1, \cdots, \bar{q}_n\}$. For $\varepsilon_1, \varepsilon_2 > 0$, define

$$\boldsymbol{u}^{\boldsymbol{\varepsilon}}_n = \sum_{i=1}^n a^{\boldsymbol{\varepsilon}}_i(t)\bar{\boldsymbol{v}}_i, \quad \boldsymbol{u}^{\boldsymbol{\varepsilon}}_{\mathrm{e},n} = \sum_{i=1}^n b^{\boldsymbol{\varepsilon}}_i(t)\bar{\boldsymbol{v}}_i, \quad \Phi^{\boldsymbol{\varepsilon}}_n = \sum_{i=1}^n c^{\boldsymbol{\varepsilon}}_i(t)\bar{q}_i$$

as the solution, for $i = 1, \ldots, n$, of the regularized system

$$((\boldsymbol{u}^{\boldsymbol{\varepsilon}}_n)', \bar{\boldsymbol{v}}_i) + \nu(\nabla \boldsymbol{u}^{\boldsymbol{\varepsilon}}_n, \nabla \bar{\boldsymbol{v}}_i) - (\Phi^{\boldsymbol{\varepsilon}}_n, \nabla\cdot\bar{\boldsymbol{v}}_i) - (\boldsymbol{u}^{\boldsymbol{\varepsilon}}_n\times\boldsymbol{B}, \bar{\boldsymbol{v}}_i) = \langle \boldsymbol{f}, \bar{\boldsymbol{v}}_i\rangle\,, \tag{19}$$

$$\varepsilon_1((\boldsymbol{u}^{\boldsymbol{\varepsilon}}_{\mathrm{e},n})', \bar{\boldsymbol{v}}_i) + \nu_{\mathrm{e}}(\nabla \boldsymbol{u}^{\boldsymbol{\varepsilon}}_{\mathrm{e},n}, \nabla \bar{\boldsymbol{v}}_i) + (\Phi^{\boldsymbol{\varepsilon}}_n, \nabla\cdot\bar{\boldsymbol{v}}_i) + (\boldsymbol{u}^{\boldsymbol{\varepsilon}}_{\mathrm{e},n}\times\boldsymbol{B}, \bar{\boldsymbol{v}}_i) = \langle \boldsymbol{f}_{\mathrm{e}}, \bar{\boldsymbol{v}}_i\rangle\,, \tag{20}$$

$$\varepsilon_1((\Phi^{\boldsymbol{\varepsilon}}_n)', \bar{q}_i) + \varepsilon_2(\nabla\Phi^{\boldsymbol{\varepsilon}}_n, \nabla\bar{q}_i) + (\nabla\cdot(\boldsymbol{u}^{\boldsymbol{\varepsilon}}_n - \boldsymbol{u}^{\boldsymbol{\varepsilon}}_{\mathrm{e},n}), \bar{q}_i) = 0, \tag{21}$$

with $\boldsymbol{u}^{\boldsymbol{\varepsilon}}_n(t=0) = P_n\boldsymbol{u}_0$, $\boldsymbol{u}^{\boldsymbol{\varepsilon}}_{\mathrm{e},n}(t=0) = \boldsymbol{0}$ and $\Phi^{\boldsymbol{\varepsilon}}_n(t=0) = 0$ and where P_n denotes the L^2 orthogonal projector onto $\boldsymbol{V}_n$ with respect to the $\boldsymbol{L}^2$ inner product. The existence and uniqueness of an approximate solution on $[0,T]$ is ensured by Picard's theorem. For $i = 1, \ldots, n$, multiply (19), (20) and (21) by $a^{\boldsymbol{\varepsilon}}_i(t)$, $b^{\boldsymbol{\varepsilon}}_i(t)$ and $c^{\boldsymbol{\varepsilon}}_i(t)$, respectively, sum over i and add the resulting equations to get

$$\begin{aligned}\frac{1}{2}\frac{d}{dt}\|\boldsymbol{u}^{\boldsymbol{\varepsilon}}_n\|^2_{\boldsymbol{L}^2} + \frac{\varepsilon_1}{2}\frac{d}{dt}\|\boldsymbol{u}^{\boldsymbol{\varepsilon}}_{\mathrm{e},n}\|^2_{\boldsymbol{L}^2} + \frac{\varepsilon_1}{2}\frac{d}{dt}\|\Phi^{\boldsymbol{\varepsilon}}_n\|^2_{L^2}\\ + \nu\|\nabla\boldsymbol{u}^{\boldsymbol{\varepsilon}}_n\|^2_{\boldsymbol{L}^2} + \nu_{\mathrm{e}}\|\nabla\boldsymbol{u}^{\boldsymbol{\varepsilon}}_{\mathrm{e},n}\|^2_{\boldsymbol{L}^2} + \varepsilon_2\|\nabla\Phi^{\boldsymbol{\varepsilon}}_n\|^2_{\boldsymbol{L}^2} = \langle \boldsymbol{f}, \boldsymbol{u}^{\boldsymbol{\varepsilon}}_n\rangle + \langle \boldsymbol{f}_{\mathrm{e}}, \boldsymbol{u}^{\boldsymbol{\varepsilon}}_{\mathrm{e},n}\rangle\end{aligned}$$

and observe that, using Poincaré's inequality,

$$\langle \boldsymbol{f}, \boldsymbol{u}_n^{\boldsymbol{\varepsilon}} \rangle \leq \frac{C_p^2+1}{2\nu} \|\boldsymbol{f}\|_{H^{-1}}^2 + \frac{\nu}{2} \|\nabla \boldsymbol{u}_n^{\boldsymbol{\varepsilon}}\|_{\boldsymbol{L}^2}^2,$$

and the same holds for $\langle \boldsymbol{f}_{\mathrm{e}}, \boldsymbol{u}_{\mathrm{e},n}^{\boldsymbol{\varepsilon}} \rangle$. Therefore,

$$\begin{aligned} &\frac{d}{dt}\|\boldsymbol{u}_n^{\boldsymbol{\varepsilon}}\|_{\boldsymbol{L}^2}^2 + \varepsilon_1 \frac{d}{dt}\|\boldsymbol{u}_{\mathrm{e},n}^{\boldsymbol{\varepsilon}}\|_{\boldsymbol{L}^2}^2 + \varepsilon_1 \frac{d}{dt}\|\Phi_n^{\boldsymbol{\varepsilon}}\|_{L^2}^2 \\ &\quad + \nu \|\nabla \boldsymbol{u}_n^{\boldsymbol{\varepsilon}}\|_{\boldsymbol{L}^2}^2 + \nu_{\mathrm{e}} \|\nabla \boldsymbol{u}_{\mathrm{e},n}^{\boldsymbol{\varepsilon}}\|_{\boldsymbol{L}^2}^2 + 2\varepsilon_2 \|\nabla \Phi_n^{\boldsymbol{\varepsilon}}\|_{\boldsymbol{L}^2}^2 \leq \frac{C}{\nu}\|\boldsymbol{f}\|_{H^{-1}}^2 + \frac{C}{\nu_{\mathrm{e}}}\|\boldsymbol{f}_{\mathrm{e}}\|_{H^{-1}}^2. \end{aligned} \tag{22}$$

We can now integrate (22) in time obtaining uniform estimates in n for the following norms:

$$\|\boldsymbol{u}_n^{\boldsymbol{\varepsilon}}\|_{L^2(0,T;\boldsymbol{H}_0^1)} \qquad \|\boldsymbol{u}_{\mathrm{e},n}^{\boldsymbol{\varepsilon}}\|_{L^2(0,T;\boldsymbol{H}_0^1)} \qquad \|\Phi_n^{\boldsymbol{\varepsilon}}\|_{L^2(0,T;H^1_{\int=0})};$$

corresponding uniform estimates in n for the time derivatives can be obtained following [29, § 7.1.2]:

$$\|(\boldsymbol{u}_n^{\boldsymbol{\varepsilon}})'\|_{L^2(0,T;\boldsymbol{H}^{-1})} \qquad \|(\boldsymbol{u}_{\mathrm{e},n}^{\boldsymbol{\varepsilon}})'\|_{L^2(0,T;\boldsymbol{H}^{-1})} \qquad \|(\Phi_n^{\boldsymbol{\varepsilon}})'\|_{L^2(0,T;(H^1_{\int=0})')}.$$

Such estimates allow us to conclude that there exists a unique solution $\boldsymbol{u}^{\boldsymbol{\varepsilon}}, \boldsymbol{u}_{\mathrm{e}}^{\boldsymbol{\varepsilon}} \in L^2(0,T;\boldsymbol{H}_0^1) \cap C^0(0,T;\boldsymbol{L}^2)$, $\Phi^{\boldsymbol{\varepsilon}} \in L^2(0,T;H^1_{\int=0}) \cap C^0(0,T;L^2)$ such that

$$\langle (\boldsymbol{u}^{\boldsymbol{\varepsilon}})', \boldsymbol{v} \rangle + \nu(\nabla \boldsymbol{u}^{\boldsymbol{\varepsilon}}, \nabla \boldsymbol{v}) - (\Phi^{\boldsymbol{\varepsilon}}, \nabla \cdot \boldsymbol{v}) - (\boldsymbol{u}^{\boldsymbol{\varepsilon}} \times \boldsymbol{B}, \boldsymbol{v}) = \langle \boldsymbol{f}, \boldsymbol{v} \rangle, \tag{23}$$

$$\varepsilon_1 \langle (\boldsymbol{u}_{\mathrm{e}}^{\boldsymbol{\varepsilon}})', \boldsymbol{v}_{\mathrm{e}} \rangle + \nu_{\mathrm{e}}(\nabla \boldsymbol{u}_{\mathrm{e}}^{\boldsymbol{\varepsilon}}, \nabla \boldsymbol{v}_{\mathrm{e}}) + (\Phi^{\boldsymbol{\varepsilon}}, \nabla \cdot \boldsymbol{v}_{\mathrm{e}}) + (\boldsymbol{u}_{\mathrm{e}}^{\boldsymbol{\varepsilon}} \times \boldsymbol{B}, \boldsymbol{v}_{\mathrm{e}}) = \langle \boldsymbol{f}_{\mathrm{e}}, \boldsymbol{v}_{\mathrm{e}} \rangle, \tag{24}$$

$$\varepsilon_1 \langle (\Phi^{\boldsymbol{\varepsilon}})', q \rangle + \varepsilon_2 (\nabla \Phi^{\boldsymbol{\varepsilon}}, \nabla q) + (\nabla \cdot (\boldsymbol{u}^{\boldsymbol{\varepsilon}} - \boldsymbol{u}_{\mathrm{e}}^{\boldsymbol{\varepsilon}}), q) = 0, \tag{25}$$

for almost every $t \in [0,T]$, for every $(\boldsymbol{v}, \boldsymbol{v}_{\mathrm{e}}, q) \in \boldsymbol{H}_0^1 \times \boldsymbol{H}_0^1 \times H^1_{\int=0}$ and satisfying the prescribed initial condition.

Let us now consider the limit $\varepsilon_1 \to 0$. Taking $(\boldsymbol{v}, \boldsymbol{v}_{\mathrm{e}}, q) = (\boldsymbol{u}^{\boldsymbol{\varepsilon}}, \boldsymbol{u}_{\mathrm{e}}^{\boldsymbol{\varepsilon}}, \Phi^{\boldsymbol{\varepsilon}})$ in (23)–(25) and proceeding as in the derivation of (22) yields

$$\begin{aligned} &\frac{d}{dt}\|\boldsymbol{u}^{\boldsymbol{\varepsilon}}\|_{\boldsymbol{L}^2}^2 + \varepsilon_1 \frac{d}{dt}\|\boldsymbol{u}_{\mathrm{e}}^{\boldsymbol{\varepsilon}}\|_{\boldsymbol{L}^2}^2 + \varepsilon_1 \frac{d}{dt}\|\Phi^{\boldsymbol{\varepsilon}}\|_{L^2}^2 \\ &\quad + \nu \|\nabla \boldsymbol{u}^{\boldsymbol{\varepsilon}}\|_{\boldsymbol{L}^2}^2 + \nu_{\mathrm{e}} \|\nabla \boldsymbol{u}_{\mathrm{e}}^{\boldsymbol{\varepsilon}}\|_{\boldsymbol{L}^2}^2 + 2\varepsilon_2 \|\nabla \Phi^{\boldsymbol{\varepsilon}}\|_{\boldsymbol{L}^2}^2 \leq \frac{C}{\nu}\|\boldsymbol{f}\|_{H^{-1}}^2 + \frac{C}{\nu_{\mathrm{e}}}\|\boldsymbol{f}_{\mathrm{e}}\|_{H^{-1}}^2, \end{aligned} \tag{26}$$

which provides uniform estimates in ε_1 for the following norms:

$$\|\boldsymbol{u}^{\boldsymbol{\varepsilon}}\|_{L^2(0,T;\boldsymbol{H}_0^1)} \quad \|(\boldsymbol{u}^{\boldsymbol{\varepsilon}})'\|_{L^2(0,T;\boldsymbol{H}^{-1})} \quad \|\boldsymbol{u}_{\mathrm{e}}^{\boldsymbol{\varepsilon}}\|_{L^2(0,T;\boldsymbol{H}_0^1)} \quad \|\Phi^{\boldsymbol{\varepsilon}}\|_{L^2(0,T;H^1_{\int=0})}.$$

Thus, for $\varepsilon_1 \to 0$, the following limits exist: $\boldsymbol{u}^{\boldsymbol{\varepsilon}} \xrightarrow{w} \boldsymbol{u}^{\varepsilon_2}$, $\boldsymbol{u}_{\mathrm{e}}^{\boldsymbol{\varepsilon}} \xrightarrow{w} \boldsymbol{u}_{\mathrm{e}}^{\varepsilon_2}$ in $L^2(0,T;\boldsymbol{H}_0^1)$, $\Phi^{\boldsymbol{\varepsilon}} \xrightarrow{w} \Phi^{\varepsilon_2}$ in $L^2(0,T;H^1_{\int=0})$ and $(\boldsymbol{u}^{\boldsymbol{\varepsilon}})' \xrightarrow{w} (\boldsymbol{u}^{\varepsilon_2})'$ in $L^2(0,T;\boldsymbol{H}^{-1})$. For an arbitrary integer N, let us now take $(\boldsymbol{v}, \boldsymbol{v}_{\mathrm{e}}, q) = (\bar{\boldsymbol{v}}_i, \bar{\boldsymbol{v}}_i, \bar{q}_i)$, for $i = 1, \ldots, N$, in (23)–(25) and, upon choosing a collection of smooth functions $\{a_i(t), b_i(t), c_i(t)\}_{i=1}^N$ such that $b_i(0) = b_i(T) = c_i(0) = c_i(T) = 0$, let us multiply each

equation by $a_i(t)$, $b_i(t)$ and $c_i(t)$, respectively, add over i and integrate in time to obtain

$$\int_0^T \left[\langle (\boldsymbol{u}^{\boldsymbol{\varepsilon}})', \boldsymbol{v}_N\rangle + \nu(\nabla \boldsymbol{u}^{\boldsymbol{\varepsilon}}, \nabla \boldsymbol{v}_N) - (\Phi^{\boldsymbol{\varepsilon}}, \nabla\cdot \boldsymbol{v}_N) - (\boldsymbol{u}^{\boldsymbol{\varepsilon}}\times \boldsymbol{B}, \boldsymbol{v}_N)\right] dt = \int_0^T \langle \boldsymbol{f}, \boldsymbol{v}_N\rangle\, dt, \quad (27)$$

$$\int_0^T \left[\varepsilon_1 \langle (\boldsymbol{u}_{\mathrm{e}}^{\boldsymbol{\varepsilon}})', \boldsymbol{v}_{\mathrm{e},N}\rangle + \nu_{\mathrm{e}}(\nabla \boldsymbol{u}_{\mathrm{e}}^{\boldsymbol{\varepsilon}}, \nabla \boldsymbol{v}_{\mathrm{e},N}) + (\Phi^{\boldsymbol{\varepsilon}}, \nabla\cdot \boldsymbol{v}_{\mathrm{e},N}) + (\boldsymbol{u}_{\mathrm{e}}^{\boldsymbol{\varepsilon}}\times \boldsymbol{B}, \boldsymbol{v}_{\mathrm{e},N})\right] dt = \int_0^T \langle \boldsymbol{f}_{\mathrm{e}}, \boldsymbol{v}_{\mathrm{e},N}\rangle\, dt, \quad (28)$$

$$\int_0^T \left[\varepsilon_1 \langle (\Phi^{\boldsymbol{\varepsilon}})', q_N\rangle + \varepsilon_2(\nabla \Phi^{\boldsymbol{\varepsilon}}, \nabla q_N) + (\nabla\cdot(\boldsymbol{u}^{\boldsymbol{\varepsilon}} - \boldsymbol{u}_{\mathrm{e}}^{\boldsymbol{\varepsilon}}), q_N)\right] dt = 0, \quad (29)$$

where we have defined

$$\boldsymbol{v}_N = \sum_{i=1}^N a_i(t)\bar{\boldsymbol{v}}_i, \quad \boldsymbol{v}_{\mathrm{e},N} = \sum_{i=1}^N b_i(t)\bar{\boldsymbol{v}}_i, \quad q_N = \sum_{i=1}^N c_i(t)\bar{q}_i. \quad (30)$$

Observe now that

$$\int_0^T \varepsilon_1 \langle (\boldsymbol{u}_{\mathrm{e}}^{\boldsymbol{\varepsilon}})', \boldsymbol{v}_{\mathrm{e},N}\rangle\, dt = -\int_0^T \varepsilon_1 (\boldsymbol{u}_{\mathrm{e}}^{\boldsymbol{\varepsilon}}, \boldsymbol{v}'_{\mathrm{e},N}) dt \le \varepsilon_1 \|\boldsymbol{u}_{\mathrm{e}}^{\boldsymbol{\varepsilon}}\|_{L^2(0,T;\boldsymbol{L}^2)} \|\boldsymbol{v}'_{\mathrm{e},N}\|_{L^2(0,T;\boldsymbol{L}^2)}$$

so that, considering the uniform bound for $\|\boldsymbol{u}_{\mathrm{e}}^{\boldsymbol{\varepsilon}}\|_{L^2(0,T;\boldsymbol{L}^2)}$ and the fact that $\boldsymbol{v}_{\mathrm{e},N}$ is fixed, this term vanishes for $\varepsilon_1 \to 0$. The same is true for the term involving $(\Phi^{\boldsymbol{\varepsilon}})'$ in (29). Passing to the limit in (27)–(29) we conclude that the limit solution satisfies

$$\int_0^T \left[\langle (\boldsymbol{u}^{\varepsilon_2})', \boldsymbol{v}_N\rangle + \nu(\nabla \boldsymbol{u}^{\varepsilon_2}, \nabla \boldsymbol{v}_N) - (\Phi^{\varepsilon_2}, \nabla\cdot \boldsymbol{v}_N) - (\boldsymbol{u}^{\varepsilon_2}\times \boldsymbol{B}, \boldsymbol{v}_N)\right] dt = \int_0^T \langle \boldsymbol{f}, \boldsymbol{v}_N\rangle\, dt, \quad (31)$$

$$\int_0^T \left[\nu_{\mathrm{e}}(\nabla \boldsymbol{u}_{\mathrm{e}}^{\varepsilon_2}, \nabla \boldsymbol{v}_{\mathrm{e},N}) + (\Phi^{\varepsilon_2}, \nabla\cdot \boldsymbol{v}_{\mathrm{e},N}) + (\boldsymbol{u}_{\mathrm{e}}^{\varepsilon_2}\times \boldsymbol{B}, \boldsymbol{v}_{\mathrm{e},N})\right] dt = \int_0^T \langle \boldsymbol{f}_{\mathrm{e}}, \boldsymbol{v}_{\mathrm{e},N}\rangle\, dt, \quad (32)$$

$$\int_0^T \left[\varepsilon_2(\nabla \Phi^{\varepsilon_2}, \nabla q_N) + (\nabla\cdot(\boldsymbol{u}^{\varepsilon_2} - \boldsymbol{u}_{\mathrm{e}}^{\varepsilon_2}), q_N)\right] dt = 0, \quad (33)$$

In fact, since functions of the form (30) are dense in $L^2(0,T;\boldsymbol{H}^1)$ and $L^2(0,T;H^1)$, we conclude that, for a.e. $t \in [0,T]$, for every $(\boldsymbol{v}, \boldsymbol{v}_{\mathrm{e}}, q) \in \boldsymbol{H}_0^1 \times \boldsymbol{H}_0^1 \times H^1_{\int=0}$,

$$\langle (\boldsymbol{u}^{\varepsilon_2})', \boldsymbol{v}\rangle + \nu(\nabla \boldsymbol{u}^{\varepsilon_2}, \nabla \boldsymbol{v}) - (\Phi^{\varepsilon_2}, \nabla\cdot \boldsymbol{v}) - (\boldsymbol{u}^{\varepsilon_2}\times \boldsymbol{B}, \boldsymbol{v}) = \langle \boldsymbol{f}, \boldsymbol{v}\rangle\,, \quad (34)$$

$$\nu_{\mathrm{e}}(\nabla \boldsymbol{u}_{\mathrm{e}}^{\varepsilon_2}, \nabla \boldsymbol{v}_{\mathrm{e}}) + (\Phi^{\varepsilon_2}, \nabla\cdot \boldsymbol{v}_{\mathrm{e}}) + (\boldsymbol{u}_{\mathrm{e}}^{\varepsilon_2}\times \boldsymbol{B}, \boldsymbol{v}_{\mathrm{e}}) = \langle \boldsymbol{f}_{\mathrm{e}}, \boldsymbol{v}_{\mathrm{e}}\rangle\,, \quad (35)$$

$$\varepsilon_2(\nabla \Phi^{\varepsilon_2}, \nabla q) + (\nabla\cdot(\boldsymbol{u}^{\varepsilon_2} - \boldsymbol{u}_{\mathrm{e}}^{\varepsilon_2}), q) = 0. \quad (36)$$

The last step is to take the limit $\varepsilon_2 \to 0$. Proceeding from (34)–(36) as done in the derivation of (26), we obtain uniform bounds in ε_2 for $\|\boldsymbol{u}^{\varepsilon_2}\|_{L^2(0,T;\boldsymbol{H}_0^1)}$, $\|(\boldsymbol{u}^{\varepsilon_2})'\|_{L^2(0,T;\boldsymbol{H}^{-1})}$ and $\|\boldsymbol{u}_{\mathrm{e}}^{\varepsilon_2}\|_{L^2(0,T;\boldsymbol{H}_0^1)}$; a uniform bound for $\|\boldsymbol{u}_{\mathrm{e}}^{\varepsilon_2}\|_{L^\infty(0,T;\boldsymbol{H}_0^1)}$ can also be obtained. A uniform bound for Φ^{ε_2} now follows from an inf-sup condition and (35). Indeed, by an inf-sup condition between $L^2_{\int=0}$ and $\boldsymbol{H}_0^1$, there exists $\beta > 0$ such that, for every $q \in L^2_{\int=0}$,

$$\beta \|q\|_{L^2} \le \sup_{0\neq \boldsymbol{v}\in \boldsymbol{H}_0^1} \frac{(q, \nabla\cdot \boldsymbol{v})}{\|\nabla \boldsymbol{v}\|_{\boldsymbol{L}^2}}.$$

From (35) we have

$$(\Phi^{\varepsilon_2}, \nabla \cdot \boldsymbol{v}_{\mathrm{e}}) \leq \left((\nu_{\mathrm{e}} + C_p^2 \|\boldsymbol{B}\|_{\boldsymbol{L}^\infty}) \|\nabla \boldsymbol{u}_{\mathrm{e}}^{\varepsilon_2}\|_{\boldsymbol{L}^2} + C_p \|\boldsymbol{f}_{\mathrm{e}}\|_{\boldsymbol{H}^{-1}}\right) \|\nabla \boldsymbol{v}_{\mathrm{e}}\|_{\boldsymbol{L}^2},$$

yielding

$$\|\Phi^{\varepsilon_2}\|_{L^2} \leq \frac{1}{\beta} \left((\nu_{\mathrm{e}} + C_p^2 \|\boldsymbol{B}\|_{\boldsymbol{L}^\infty}) \|\nabla \boldsymbol{u}_{\mathrm{e}}^{\varepsilon_2}\|_{\boldsymbol{L}^2} + C_p \|\boldsymbol{f}_{\mathrm{e}}\|_{\boldsymbol{H}^{-1}}\right)$$

where we can use the uniform bound for $\|\boldsymbol{u}_{\mathrm{e}}^{\varepsilon_2}\|_{L^\infty(0,T;\boldsymbol{H}_0^1)}$. Hence, for $\varepsilon_2 \to 0$, the following limits exist: $\boldsymbol{u}^{\varepsilon_2} \xrightarrow{w} \boldsymbol{u}$, $\boldsymbol{u}_{\mathrm{e}}^{\varepsilon_2} \xrightarrow{w} \boldsymbol{u}_{\mathrm{e}}$ in $L^2(0,T;\boldsymbol{H}_0^1)$, $\Phi^{\varepsilon_2} \xrightarrow{w} \Phi$ in $L^2(0,T;L^2_{\int=0})$ and $(\boldsymbol{u}^{\varepsilon_2})' \xrightarrow{w} \boldsymbol{u}'$ in $L^2(0,T;\boldsymbol{H}^{-1})$. Let us now fix $(\boldsymbol{v}_c, \boldsymbol{v}_{\mathrm{e},c}, q_c) \in \boldsymbol{H}_0^1 \times \boldsymbol{H}_0^1 \times C_c^\infty(\Omega) \cap L^2_{\int=0}$ in (34)–(36). Observe now that

$$\varepsilon_2(\nabla \Phi^{\varepsilon_2}, \nabla q_c) = -\varepsilon_2(\Phi^{\varepsilon_2}, \Delta q_c) \leq \varepsilon_2 \|\Phi^{\varepsilon_2}\|_{L^2} \|\Delta q_c\|_{L^2}$$

so that, considering the uniform bound for $\|\Phi^{\varepsilon_2}\|_{L^2}$ and the fact that q_c is fixed, this term vanishes for $\varepsilon_2 \to 0$. Passing to the limit in (34)–(36), we conclude that the limit solution satisfies

$$\langle \boldsymbol{u}', \boldsymbol{v}_c \rangle + \nu(\nabla \boldsymbol{u}, \nabla \boldsymbol{v}_c) - (\Phi, \nabla \cdot \boldsymbol{v}_c) - (\boldsymbol{u} \times \boldsymbol{B}, \boldsymbol{v}_c) = \langle \boldsymbol{f}, \boldsymbol{v}_c \rangle, \tag{37}$$

$$\nu_{\mathrm{e}}(\nabla \boldsymbol{u}_{\mathrm{e}}, \nabla \boldsymbol{v}_{\mathrm{e},c}) + (\Phi, \nabla \cdot \boldsymbol{v}_{\mathrm{e},c}) + (\boldsymbol{u}_{\mathrm{e}} \times \boldsymbol{B}, \boldsymbol{v}_{\mathrm{e},c}) = \langle \boldsymbol{f}_{\mathrm{e}}, \boldsymbol{v}_{\mathrm{e},c} \rangle, \tag{38}$$

$$(\nabla \cdot (\boldsymbol{u} - \boldsymbol{u}_{\mathrm{e}}), q_c) = 0. \tag{39}$$

In fact, thanks to the density of $C_c^\infty(\Omega) \cap L^2_{\int=0}$ in $L^2_{\int=0}$, (37)–(39) hold for every $(\boldsymbol{v}, \boldsymbol{v}_{\mathrm{e}}, q) \in \boldsymbol{H}_0^1 \times \boldsymbol{H}_0^1 \times L^2_{\int=0}$, thus concluding the proof. □

We now turn our attention to the existence of a strong solution of (16)–(18). A weak solution will be strong if

$$\boldsymbol{u} \in L^\infty(0,T;\boldsymbol{H}_0^1) \cap L^2(0,T;\boldsymbol{H}^2 \cap \boldsymbol{H}_0^1), \qquad \boldsymbol{u}' \in L^2(0,T;\boldsymbol{L}^2),$$

$$\boldsymbol{u}_{\mathrm{e}} \in L^2(0,T;\boldsymbol{H}^2 \cap \boldsymbol{H}_0^1),$$

and

$$\Phi \in L^2(0,T;H^1_{\int=0}).$$

Theorem 2. *Let Ω be an open bounded set either of class $C^{1,1}$ or Lipschitz continuous and convex. Assume $\boldsymbol{f}, \boldsymbol{f}_{\mathrm{e}} \in L^2(0,T;\boldsymbol{L}^2)$ and $\boldsymbol{u}_0 \in \boldsymbol{H}_0^1$. Then (16)–(18) has a unique strong solution on $[0,T]$.*

Proof. Let us first consider the regularized problem (34)–(36). Upon rewriting (36) as

$$\varepsilon_2(\nabla \Phi^{\varepsilon_2}, \nabla q) = (h^{\Phi^{\varepsilon_2}}, q),$$

with $h^{\Phi^{\varepsilon_2}} = -\nabla \cdot (\boldsymbol{u}^{\varepsilon_2} - \boldsymbol{u}_{\mathrm{e}}^{\varepsilon_2})$, using the fact that $\boldsymbol{u}^{\varepsilon_2}, \boldsymbol{u}_{\mathrm{e}}^{\varepsilon_2} \in \boldsymbol{H}_0^1$ and standard regularity results [29, § 6.3.2] (see also [30] for the case with minimal domain regularity), we conlcude that $\Phi^{\varepsilon_2} \in H^2_{\int=0}$ for a.e. $t \in (0,T)$, and also $\Phi^{\varepsilon_2} \in L^2(0,T;H^2_{\int=0})$. By the same argument we can rewrite (35) as

$$\nu_{\mathrm{e}}(\nabla \boldsymbol{u}_{\mathrm{e}}^{\varepsilon_2}, \nabla \boldsymbol{v}_{\mathrm{e}}) = (\boldsymbol{h}^{\boldsymbol{u}_{\mathrm{e}}^{\varepsilon_2}}, \boldsymbol{v}_{\mathrm{e}})$$

with $\boldsymbol{h}^{\boldsymbol{u}_{\mathrm{e}}^{\varepsilon_2}} = \nabla\Phi^{\varepsilon_2} - \boldsymbol{u}_{\mathrm{e}}^{\varepsilon_2}\times\boldsymbol{B} + \boldsymbol{f}_{\mathrm{e}}$ and conclude that $\boldsymbol{u}_{\mathrm{e}}^{\varepsilon_2} \in L^2(0,T;\boldsymbol{H}^2\cap\boldsymbol{H}_0^1)$. Finally, regarding (34) as a heat equation

$$\langle(\boldsymbol{u}^{\varepsilon_2})',\boldsymbol{v}\rangle + \nu(\nabla\boldsymbol{u}^{\varepsilon_2},\nabla\boldsymbol{v}) = (\boldsymbol{h}^{\boldsymbol{u}^{\varepsilon_2}},\boldsymbol{v})$$

with $\boldsymbol{h}^{\boldsymbol{u}^{\varepsilon_2}} = -\nabla\Phi^{\varepsilon_2} + \boldsymbol{u}^{\varepsilon_2}\times\boldsymbol{B} + \boldsymbol{f}$, using again standard regularity results [29, § 7.1.3], we conclude that $\boldsymbol{u}^{\varepsilon_2} \in L^2(0,T;\boldsymbol{H}^2\cap\boldsymbol{H}_0^1)$ and $(\boldsymbol{u}^{\varepsilon_2})' \in L^2(0,T;\boldsymbol{L}^2)$. These results imply that (34)–(36) hold in a strong sense, i.e.

$$(\boldsymbol{u}^{\varepsilon_2})' + \nabla\Phi^{\varepsilon_2} - \boldsymbol{u}^{\varepsilon_2}\times\boldsymbol{B} - \nu\Delta\boldsymbol{u}^{\varepsilon_2} = \boldsymbol{f}, \tag{40}$$

$$-\nabla\Phi^{\varepsilon_2} + \boldsymbol{u}_{\mathrm{e}}^{\varepsilon_2}\times\boldsymbol{B} - \nu_{\mathrm{e}}\Delta\boldsymbol{u}_{\mathrm{e}}^{\varepsilon_2} = \boldsymbol{f}_{\mathrm{e}}, \tag{41}$$

$$-\varepsilon_2\Delta\Phi^{\varepsilon_2} + \nabla\cdot(\boldsymbol{u}^{\varepsilon_2} - \boldsymbol{u}_{\mathrm{e}}^{\varepsilon_2}) = 0 \tag{42}$$

with $\boldsymbol{u}^{\varepsilon_2} = \boldsymbol{u}_{\mathrm{e}}^{\varepsilon_2} = 0$ and $\boldsymbol{n}\cdot\nabla\Phi^{\varepsilon_2} = 0$ on $\partial\Omega$. We can thus multiply each equation by $-\Delta\boldsymbol{u}^{\varepsilon_2}$, $-\Delta\boldsymbol{u}_{\mathrm{e}}^{\varepsilon_2}$, $-\Delta\Phi^{\varepsilon_2}$, respectively, integrate and add obtaining

$$\begin{aligned}\frac{1}{2}\frac{d}{dt}\|\nabla\boldsymbol{u}^{\varepsilon_2}\|_{\boldsymbol{L}^2}^2 + \nu\|\Delta\boldsymbol{u}^{\varepsilon_2}\|_{\boldsymbol{L}^2}^2 + \nu_{\mathrm{e}}\|\Delta\boldsymbol{u}_{\mathrm{e}}^{\varepsilon_2}\|_{\boldsymbol{L}^2}^2 + \varepsilon_2\|\Delta\Phi^{\varepsilon_2}\|_{L^2}^2 \\ = -(\boldsymbol{f} + \boldsymbol{u}^{\varepsilon_2}\times\boldsymbol{B},\Delta\boldsymbol{u}^{\varepsilon_2}) - (\boldsymbol{f}_{\mathrm{e}} - \boldsymbol{u}_{\mathrm{e}}^{\varepsilon_2}\times\boldsymbol{B},\Delta\boldsymbol{u}_{\mathrm{e}}^{\varepsilon_2}).\end{aligned} \tag{43}$$

Then we have

$$(\boldsymbol{f} + \boldsymbol{u}^{\varepsilon_2}\times\boldsymbol{B},\Delta\boldsymbol{u}^{\varepsilon_2}) \le \frac{\nu}{2}\|\Delta\boldsymbol{u}^{\varepsilon_2}\|_{\boldsymbol{L}^2}^2 + \frac{1}{\nu}\left(\|\boldsymbol{f}\|_{\boldsymbol{L}^2}^2 + \|\boldsymbol{B}\|_{\boldsymbol{L}^\infty}^2\|\boldsymbol{u}^{\varepsilon_2}\|_{\boldsymbol{L}^2}^2\right)$$

and an analogous relation for $\boldsymbol{u}_{\mathrm{e}}^{\varepsilon_2}$. Using these realtions in (43) and integrating in time we conclude, thanks to the uniform bounds for $\|\boldsymbol{u}^{\varepsilon_2}\|_{\boldsymbol{L}^2}$, $\|\boldsymbol{u}_{\mathrm{e}}^{\varepsilon_2}\|_{\boldsymbol{L}^2}$ and $\|\boldsymbol{u}_0^{\varepsilon_2}\|_{\boldsymbol{H}_0^1}$, that $\boldsymbol{u},\boldsymbol{u}_{\mathrm{e}} \in L^2(0,T;\boldsymbol{H}^2\cap\boldsymbol{H}_0^1)$ and $\boldsymbol{u} \in L^\infty(0,T;\boldsymbol{H}_0^1)$. Let us now rewrite (17), (18) as a generalized Stokes problem

$$\begin{aligned}\nu_{\mathrm{e}}(\nabla\boldsymbol{u}_{\mathrm{e}},\nabla\boldsymbol{v}_{\mathrm{e}}) + (\Phi,\nabla\cdot\boldsymbol{v}_{\mathrm{e}}) &= (\boldsymbol{h}^{\boldsymbol{u}_{\mathrm{e}}},\boldsymbol{v}_{\mathrm{e}}),\\ (\nabla\cdot\boldsymbol{u}_{\mathrm{e}},q) &= (h^{\Phi},q)\end{aligned}$$

with $\boldsymbol{h}^{\boldsymbol{u}_{\mathrm{e}}} = \boldsymbol{f}_{\mathrm{e}} - \boldsymbol{u}_{\mathrm{e}}\times\boldsymbol{B}$ and $h^{\Phi} = \nabla\cdot\boldsymbol{u}$. Standard regularity results [31], proposition 2.2 of chapter 1, imply that $\Phi \in H^1_{\int=0}$ for a.e. $t \in (0,T)$ and, integrating in time, $\Phi \in L^2(0,T;H^1_{\int=0})$. Finally, multiplying (40) by $(\boldsymbol{u}^{\varepsilon_2})'$ yields

$$\|(\boldsymbol{u}^{\varepsilon_2})'\|_{\boldsymbol{L}^2}^2 + \nu\frac{d}{dt}\|\nabla\boldsymbol{u}^{\varepsilon_2}\|_{\boldsymbol{L}^2}^2 \le 2\|\boldsymbol{f} - \nabla\Phi^{\varepsilon_2} + \boldsymbol{u}^{\varepsilon_2}\times\boldsymbol{B}\|_{\boldsymbol{L}^2}^2.$$

Integrating in time and passing to the limit using the previous results provides $\boldsymbol{u}' \in L^2(0,T;\boldsymbol{L}^2)$, thus completing the proof. □

5 Finite element discretization

In this section, we consider the spatial discretization of (16)–(18). Throughout this section, we assume the following hypothesis.

(H1) Let Ω be a convex polyhedral domain and let $\mathcal{T}_h$ be a regular tessellations of Ω such that $\overline{\Omega} = \cup_{K\in\mathcal{T}_h}K$. Moreover, let $\boldsymbol{f},\boldsymbol{f}_{\mathrm{e}} \in L^2(0,T;\boldsymbol{L}^2)$ and $\boldsymbol{u}_0 \in \boldsymbol{H}_0^1$.

(H2) Let $\boldsymbol{V}_h$, Q_h be two conforming finite-dimensional spaces on $\mathcal{T}_h$ such that $\boldsymbol{V}_h \subset \boldsymbol{H}^1_0$, and $Q_h \subset L^2_{\int=0}$.

(H3) The pairs $\boldsymbol{V}_h, Q_h$ are assumed to be uniformly compatible, i.e. there exists $\beta > 0$, independent of h, such that

$$\inf_{0\neq q_h\in Q_h} \sup_{0\neq \boldsymbol{v}_h\in \boldsymbol{V}_h} \frac{(q_h, \nabla\cdot \boldsymbol{v}_h)}{\|\boldsymbol{v}_h\|_{\boldsymbol{H}^1_0}\|q_h\|_{L^2}} \geq \beta. \tag{44}$$

(H4) The spaces $\boldsymbol{V}_h, Q_h$ are endowed with interpolation properties, i.e. there exists $C_{\rm app} > 0$, independent of h, such that, for every $\boldsymbol{v} \in \boldsymbol{H}^2$, $q \in L^2$,

$$\inf_{\boldsymbol{v}_h\in\boldsymbol{V}_h} \{\|\boldsymbol{v} - \boldsymbol{v}_h\|_{\boldsymbol{L}^2} + h\|\boldsymbol{v} - \boldsymbol{v}_h\|_{\boldsymbol{H}^1}\} \leq C_{\rm app} h^2 \|\boldsymbol{v}\|_{\boldsymbol{H}^2},$$

and

$$\inf_{q_h\in Q_h} \|q - q_h\|_{L^2} \leq C_{\rm app} h \|q\|_{H^1}.$$

The finite element discretization of (16)–(18) reads: find $\boldsymbol{u}_h, \boldsymbol{u}_{{\rm e}\,h}, \Phi_h$ such that, for each $t \in (0, T]$,

$$\frac{d}{dt}(\boldsymbol{u}_h, \boldsymbol{v}_h) + \nu(\nabla\boldsymbol{u}_h, \nabla\boldsymbol{v}_h) - (\Phi_h, \nabla\cdot\boldsymbol{v}_h) - (\boldsymbol{u}_h\times\boldsymbol{B}, \boldsymbol{v}_h) = (\boldsymbol{f}, \boldsymbol{v}_h), \tag{45}$$

$$\nu_{\rm e}(\nabla\boldsymbol{u}_{{\rm e}\,h}, \nabla\boldsymbol{v}_{{\rm e}\,h}) + (\Phi_h, \nabla\cdot\boldsymbol{v}_{{\rm e}\,h}) + (\boldsymbol{u}_{{\rm e}\,h}\times\boldsymbol{B}, \boldsymbol{v}_{{\rm e}\,h}) = (\boldsymbol{f}_{\rm e}, \boldsymbol{v}_{{\rm e}\,h}), \tag{46}$$

$$(\nabla\cdot(\boldsymbol{u}_h - \boldsymbol{u}_{{\rm e}\,h}), q_h) = 0, \tag{47}$$

for all $(\boldsymbol{v}_h, \boldsymbol{v}_{{\rm e}\,h}, q_h) \in \boldsymbol{V}_h \times \boldsymbol{V}_h \times Q_h$, with

$$\boldsymbol{u}_h(t=0) = \boldsymbol{u}_{h\,0},$$

where $\boldsymbol{u}_{h\,0} \in \boldsymbol{V}_h$ is an approximation of $\boldsymbol{u}_0$. Well-posedness of this finite element formulation is ensured by the following result.

Theorem 3. *There exists a unique solution $(\boldsymbol{u}_h, \boldsymbol{u}_{{\rm e}\,h}, \Phi_h)$ of (45)–(47).*

Proof. In (45)–(47), we can express $\boldsymbol{u}_{{\rm e}\,h}$ and Φ_h as continuous functions of $\boldsymbol{u}_h$ (thanks to the inf-sup condition). Substituting these expressions in (45) results in a system of ordinary differential equations; the existence and uniqueness of a solution on $[0, T]$ is then ensured by Picard's theorem. □

Convergence of the finite element solution to the analytic one is proven in the following result.

Theorem 4. *Let $\boldsymbol{u}, \boldsymbol{u}_{\rm e}, \Phi$ be the unique strong solution of (16)–(18) and let $\boldsymbol{u}_h, \boldsymbol{u}_{{\rm e}\,h}, \Phi_h$ be the finite element solution of (45)–(47). Then there exists a constant C, depending on the problem coefficients and $\|\boldsymbol{u}\|_{\boldsymbol{H}^2}$, $\|\boldsymbol{u}_{\rm e}\|_{\boldsymbol{H}^2}$ and $\|\Phi\|_{H^1_{\int=0}}$, such that*

$$\|\boldsymbol{u} - \boldsymbol{u}_h\|_{L^2(0,T;\boldsymbol{H}^1_0)} + \|\boldsymbol{u}_{\rm e} - \boldsymbol{u}_{{\rm e}\,h}\|_{L^2(0,T;\boldsymbol{H}^1_0)} + \|\Phi - \Phi_h\|_{L^2(0,T;L^2_{\int=0})} \leq Ch. \tag{48}$$

Proof. The proof is similar to the one described in [32, Prop. 11.2.1]. Combining (16)–(18) and (45)–(47) we obtain

$$\langle (\boldsymbol{e_u})', \boldsymbol{v}_h\rangle + \nu(\nabla \boldsymbol{e_u}, \nabla \boldsymbol{v}_h) - (e_\Phi, \nabla\cdot \boldsymbol{v}_h) - (\boldsymbol{e_u}\times \boldsymbol{B}, \boldsymbol{v}_h) = 0, \tag{49}$$

$$\nu_{\rm e}(\nabla \boldsymbol{e}_{\boldsymbol{u}_{\rm e}}, \nabla \boldsymbol{v}_{{\rm e}\,h}) + (e_\Phi, \nabla\cdot \boldsymbol{v}_{{\rm e}\,h}) + (\boldsymbol{e}_{\boldsymbol{u}_{\rm e}}\times \boldsymbol{B}, \boldsymbol{v}_{{\rm e}\,h}) = 0, \tag{50}$$

$$(\nabla\cdot (\boldsymbol{e_u} - \boldsymbol{e}_{\boldsymbol{u}_{\rm e}}), q_h) = 0, \tag{51}$$

with $\boldsymbol{e_u} = \boldsymbol{u} - \boldsymbol{u}_h$, with $\boldsymbol{e}_{\boldsymbol{u}_{\rm e}} = \boldsymbol{u}_{\rm e} - \boldsymbol{u}_{{\rm e}\,h}$ and $e_\Phi = \Phi - \Phi_h$. Observe now that, thanks to hypothesis (H1), $\boldsymbol{u}, \boldsymbol{u}_{\rm e}, \Phi$ is a strong solution and thus it is possible to choose $\boldsymbol{u}_{h\,I} \in \boldsymbol{V}_h$ such that the approximation error $\boldsymbol{\eta_u} = \boldsymbol{u} - \boldsymbol{u}_{h\,I}$ satisfies the estimates of hypothesis (H4); a possible choice is taking $\boldsymbol{u}_{h\,I} = P_h\boldsymbol{u}$, where P_h denotes the L^2 orthogonal projector onto $\boldsymbol{V}_h$ (see [33, § 1.6.3]). Take then $\boldsymbol{v}_h = \boldsymbol{\xi_u} = \boldsymbol{u}_{h\,I} - \boldsymbol{u}_h$ in (49) and similarly for $\boldsymbol{v}_{{\rm e}\,h}$ and q_h, obtaining

$$\begin{aligned}
\langle (\boldsymbol{e_u})', \boldsymbol{e_u}\rangle + \nu(\nabla \boldsymbol{e_u}, \nabla \boldsymbol{e_u}) &- (e_\Phi, \nabla\cdot \boldsymbol{e_u})\\
&= \langle (\boldsymbol{e_u})', \boldsymbol{\eta_u}\rangle + \nu(\nabla \boldsymbol{e_u}, \nabla \boldsymbol{\eta_u}) - (e_\Phi, \nabla\cdot \boldsymbol{\eta_u}) - (\boldsymbol{e_u}\times \boldsymbol{B}, \boldsymbol{\eta_u}),\\
\nu_{\rm e}(\nabla \boldsymbol{e}_{\boldsymbol{u}_{\rm e}}, \nabla \boldsymbol{e}_{\boldsymbol{u}_{\rm e}}) &+ (e_\Phi, \nabla\cdot \boldsymbol{e}_{\boldsymbol{u}_{\rm e}})\\
&= \nu_{\rm e}(\nabla \boldsymbol{e}_{\boldsymbol{u}_{\rm e}}, \nabla \boldsymbol{\eta}_{\boldsymbol{v}_{\rm e}}) + (e_\Phi, \nabla\cdot \boldsymbol{\eta}_{\boldsymbol{v}_{\rm e}}) + (\boldsymbol{e}_{\boldsymbol{u}_{\rm e}}\times \boldsymbol{B}, \boldsymbol{\eta}_{\boldsymbol{v}_{\rm e}}),\\
(\nabla\cdot (\boldsymbol{e_u} - \boldsymbol{e}_{\boldsymbol{u}_{\rm e}}), e_\Phi) &= (\nabla\cdot (\boldsymbol{e_u} - \boldsymbol{e}_{\boldsymbol{u}_{\rm e}}), \eta_\Phi),
\end{aligned}$$

and add these equations obtaining,

$$\begin{aligned}
\frac{1}{2}\frac{d}{dt}\|\boldsymbol{e_u}\|^2_{\boldsymbol{L}^2} &+ \nu\|\nabla \boldsymbol{e_u}\|^2_{\boldsymbol{L}^2} + \nu_{\rm e}\|\nabla \boldsymbol{e}_{\boldsymbol{u}_{\rm e}}\|^2_{\boldsymbol{L}^2}\\
&= \frac{1}{2}\frac{d}{dt}\|\boldsymbol{\eta_u}\|^2_{\boldsymbol{L}^2} + \nu(\nabla \boldsymbol{e_u}, \nabla \boldsymbol{\eta_u}) - (e_\Phi, \nabla\cdot \boldsymbol{\eta_u}) - (\boldsymbol{e_u}\times \boldsymbol{B}, \boldsymbol{\eta_u}),\\
&\quad + \nu_{\rm e}(\nabla \boldsymbol{e}_{\boldsymbol{u}_{\rm e}}, \nabla \boldsymbol{\eta}_{\boldsymbol{v}_{\rm e}}) + (e_\Phi, \nabla\cdot \boldsymbol{\eta}_{\boldsymbol{v}_{\rm e}}) + (\boldsymbol{e}_{\boldsymbol{u}_{\rm e}}\times \boldsymbol{B}, \boldsymbol{\eta}_{\boldsymbol{v}_{\rm e}}),\\
&\quad + (\nabla\cdot (\boldsymbol{e_u} - \boldsymbol{e}_{\boldsymbol{u}_{\rm e}}), \eta_\Phi),
\end{aligned} \tag{52}$$

where we have used

$$\langle (\boldsymbol{e_u})', \boldsymbol{\eta_u}\rangle = \langle (\boldsymbol{\eta_u})', \boldsymbol{\eta_u}\rangle + ((\boldsymbol{\xi_u})', \boldsymbol{\eta_u}) = \frac{1}{2}\frac{d}{dt}\|\boldsymbol{\eta_u}\|^2_{\boldsymbol{L}^2},$$

thanks to $(\boldsymbol{\xi_u})' \in \boldsymbol{V}_h$ and the definition of the L^2 projector.

The first step to estimate the right-hand-side of this relation is now using the discrete compatibility condition (44) to estimate $\|\xi_\Phi\|_{L^2}$ from the error equation (50). Indeed, (44) implies

$$\begin{aligned}
\beta\|\xi_\Phi\|_{L^2} &\le \sup_{0\neq \boldsymbol{v}_h\in \boldsymbol{V}_h} \frac{(\xi_\Phi, \nabla\cdot \boldsymbol{v}_h)}{\|\boldsymbol{v}_h\|_{\boldsymbol{H}^1_0}}\\
&\le \sup_{0\neq \boldsymbol{v}_h\in \boldsymbol{V}_h} \frac{(e_\Phi, \nabla\cdot \boldsymbol{v}_h) - (\eta_\Phi, \nabla\cdot \boldsymbol{v}_h)}{\|\boldsymbol{v}_h\|_{\boldsymbol{H}^1_0}}\\
&\le \|\eta_\Phi\|_{L^2} + \sup_{0\neq \boldsymbol{v}_h\in \boldsymbol{V}_h} \frac{(e_\Phi, \nabla\cdot \boldsymbol{v}_h)}{\|\boldsymbol{v}_h\|_{\boldsymbol{H}^1_0}}
\end{aligned}$$

and from (50)

$$\begin{aligned}
(e_\Phi, \nabla\cdot \boldsymbol{v}_h) &= -\nu_{\rm e}(\nabla \boldsymbol{e}_{\boldsymbol{u}_{\rm e}}, \nabla \boldsymbol{v}_h) - (\boldsymbol{e}_{\boldsymbol{u}_{\rm e}}\times \boldsymbol{B}, \boldsymbol{v}_h)\\
&\le \left(\nu_{\rm e} + \|\boldsymbol{B}\|_{\boldsymbol{L}^\infty} C_P^2\right)\|\nabla \boldsymbol{e}_{\boldsymbol{u}_{\rm e}}\|_{\boldsymbol{L}^2}\|\nabla \boldsymbol{v}_h\|_{\boldsymbol{L}^2},
\end{aligned}$$

so that

$$\beta\|\xi_\Phi\|_{L^2} \le \|\eta_\Phi\|_{L^2} + \left(\nu_\mathrm{e} + \|\boldsymbol{B}\|_{\boldsymbol{L}^\infty} C_P^2\right) \|\nabla \boldsymbol{e}_{\boldsymbol{u}_\mathrm{e}}\|_{\boldsymbol{L}^2}. \tag{53}$$

Let us now proceed to estimate the right-hand-side of (52). We have

$$\begin{aligned}\nu(\nabla \boldsymbol{e}_{\boldsymbol{u}}, \nabla \boldsymbol{\eta}_{\boldsymbol{u}}) - (\boldsymbol{e}_{\boldsymbol{u}} \times \boldsymbol{B}, \boldsymbol{\eta}_{\boldsymbol{u}}) + (\nabla \cdot \boldsymbol{e}_{\boldsymbol{u}}, \eta_\Phi) \\ \le \frac{3}{2}\epsilon_1 \|\nabla \boldsymbol{e}_{\boldsymbol{u}}\|^2_{\boldsymbol{L}^2} + \frac{\nu^2}{2\epsilon_1}\|\nabla \boldsymbol{\eta}_{\boldsymbol{u}}\|^2_{\boldsymbol{L}^2} + \frac{C_P^2 \|\boldsymbol{B}\|^2_{\boldsymbol{L}^\infty}}{2\epsilon_1}\|\boldsymbol{\eta}_{\boldsymbol{u}}\|^2_{\boldsymbol{L}^2} + \frac{1}{2\epsilon_1}\|\eta_\Phi\|^2_{\boldsymbol{L}^2}\end{aligned}$$

for an arbitrary constant ϵ_1 to be fixed later; a similar estimate holds for the corresponding terms in $\boldsymbol{u}_\mathrm{e}$, for another arbitrary constant ϵ_2. Also,

$$\begin{aligned}(e_\Phi, \nabla \cdot \boldsymbol{\eta}_{\boldsymbol{u}}) &= (\eta_\Phi + \xi_\Phi, \nabla \cdot \boldsymbol{\eta}_{\boldsymbol{u}}) \\ &\le \left(\|\eta_\Phi\|_{L^2} + \|\xi_\Phi\|_{L^2}\right) \|\nabla \boldsymbol{\eta}_{\boldsymbol{u}}\|_{\boldsymbol{L}^2} \\ &\le \frac{\epsilon_3}{2}\|\xi_\Phi\|^2_{L^2} + \frac{1}{2}\left(1 + \frac{1}{\epsilon_3}\right)\|\nabla \boldsymbol{\eta}_{\boldsymbol{u}}\|^2_{\boldsymbol{L}^2} + \frac{1}{2}\|\eta_\Phi\|^2_{L^2};\end{aligned}$$

an analogous result holds for $(e_\Phi, \nabla \cdot \boldsymbol{\eta}_{\boldsymbol{u}_\mathrm{e}})$. Combing these estimates, and using (53), yields from (52)

$$\begin{aligned}&\frac{d}{dt}\|\boldsymbol{e}_{\boldsymbol{u}}\|^2_{\boldsymbol{L}^2} + \nu\|\nabla \boldsymbol{e}_{\boldsymbol{u}}\|^2_{\boldsymbol{L}^2} + \nu_\mathrm{e}\|\nabla \boldsymbol{e}_{\boldsymbol{u}_\mathrm{e}}\|^2_{\boldsymbol{L}^2} \\ &\qquad \le \frac{d}{dt}\|\boldsymbol{\eta}_{\boldsymbol{u}}\|^2_{\boldsymbol{L}^2} + C_1\|\nabla \boldsymbol{\eta}_{\boldsymbol{u}}\|^2_{\boldsymbol{L}^2} + C_2\|\nabla \boldsymbol{\eta}_{\boldsymbol{u}_\mathrm{e}}\|^2_{\boldsymbol{L}^2} + C_3\|\eta_\Phi\|^2_{L^2},\end{aligned} \tag{54}$$

where

$$C_1 = 1 + \frac{\nu^2 + \|\boldsymbol{B}\|^2_{\boldsymbol{L}^\infty} C_P^4}{\epsilon_1} + \frac{1}{\epsilon_3}, \qquad C_2 = 1 + \frac{\nu_\mathrm{e}^2 + \|\boldsymbol{B}\|^2_{\boldsymbol{L}^\infty} C_P^4}{\epsilon_2} + \frac{1}{\epsilon_3},$$

and

$$C_3 = 2 + \frac{1}{\epsilon_1} + \frac{1}{\epsilon_1} + \frac{4\epsilon_3}{\beta^2},$$

with

$$\epsilon_1 = \frac{\nu}{6}, \qquad \epsilon_2 = \frac{\nu_\mathrm{e}}{6}, \qquad \epsilon_3 = \frac{\nu_\mathrm{e}\beta^2}{8}\left(\nu_\mathrm{e} + \|\boldsymbol{B}\|_{\boldsymbol{L}^\infty} C_P^2\right)^{-2}.$$

Integrating (54) in time and considering the approximation properties (H4) now yields

$$\|\boldsymbol{e}_{\boldsymbol{u}}(t)\|^2_{\boldsymbol{L}^2} + \nu\|\nabla \boldsymbol{e}_{\boldsymbol{u}}\|^2_{L^2(0,T;\boldsymbol{L}^2)} + \nu_\mathrm{e}\|\nabla \boldsymbol{e}_{\boldsymbol{u}_\mathrm{e}}\|^2_{L^2(0,T;\boldsymbol{L}^2)} \le \|\boldsymbol{e}_{\boldsymbol{u}}(0)\|^2_{\boldsymbol{L}^2} + Ch^2, \tag{55}$$

where C is a function of the problem coefficients and $\|\boldsymbol{u}\|_{\boldsymbol{H}^2}$, $\|\boldsymbol{u}_\mathrm{e}\|_{\boldsymbol{H}^2}$ and $\|\Phi\|_{H^1_{f=0}}$. The thesis follows from (55) and (53). □

6 Computational aspects

The previous sections § 4 and § 5 consider the continuous and the discrete problems, respectively, in their general form. In the present section, the finite element formulation is specialized in a way that suites the problem under investigation. In particular, this amounts to specifying: the computational grid, the finite element spaces, the complete space-time discretization and a solution procedure for the linear system. While the previous sections address both the two and the three-dimensional cases, we restrict our attention here to the two-dimensional one.

6.1 Computational grid and finite element spaces

As discussed in § 3, the magnetic field defines the parallel and perpendicular directions. Since the Lorentz force, which is the dominating term, only acts in the perpendicular direction, the presence of $\boldsymbol{B}$ results in a strong anisotropy. Such anisotropy is relevant for the numerical discretization for two reasons: first of all the computational grid should not introduce any numerical coupling between parallel and perpendicular gradients and second the representation of the vector fields should not introduce any numerical coupling between parallel and perpendicular components. A common practice is addressing both of these issues at the same time by introducing a curvilinear coordinate system in the poloidal plane where one axis is directed along the magnetic surfaces. In fact, this implies that a Cartesian grid in the coordinate space is aligned with the flux surfaces, addressing the first issue, while at the same time the contravariant vector representation induced by the coordinates naturally decouples the parallel and perpendicular directions, hence addressing the second issue. The difficulty in this approach is the choice of the curvilinear coordinate system: aligning one axis with the parallel direction typically can not be done globally and multiple patches must be introduced; another drawback is that both local grid refinement and resolving the boundary of the domain become nontrivial problems.

Here, we consider an alternative approach where the two issues mentioned above are dealt with separately: grid alignment in the sense of [10] (see also § 7) is made possible by the use of a fully unstructured grid composed of both triangles and quadrilaterals; at the same time, spurious coupling of parallel and perpendicular vector components is avoided through a careful construction of the vector finite element space $\boldsymbol{V}_h$. This combination avoids the difficulty of the multipatch approach, and in particular allows local grid refinement, good overall grid regularity and accurate representation of the domain boundaries.

Given thus $\tilde{\Omega} \in \mathbb{R}^2$ as described in § 3, let $\tilde{\mathcal{T}}_h$ be a regular tessellation of $\tilde{\Omega}$ composed of triangular and quadrilateral elements such that $\bar{\tilde{\Omega}} = \cup_{\tilde{K} \in \tilde{\mathcal{T}}_h} \tilde{K}$. The finite element space for the electrostatic potential is now

$$Q_h = \left\{ q_h \in H^1_{\int=0}(\tilde{\Omega}) \quad | \quad q_h|_{\tilde{K}} \in \mathbb{X}_1(\tilde{K}), \quad \forall \tilde{K} \in \tilde{\mathcal{T}}_h \right\},$$

where $\mathbb{X}_1(\tilde{K})$ is the space of affine and bilinear functions on $\tilde{K}$ for triangular and quadrilateral elements, respectively. To define the vector space $\boldsymbol{V}_h$, let us first introduce

$$V_h = \left\{ v_h \in H^1_0(\tilde{\Omega}) \quad | \quad v_h|_{\tilde{K}} \in \mathbb{Y}_{\text{1-iso-2}}(\tilde{K}), \quad \forall \tilde{K} \in \tilde{\mathcal{T}}_h \right\},$$

where $\mathbb{Y}_{\text{1-iso-2}}(\tilde{K})$ is the space of the $\mathbb{P}_1$-iso-$\mathbb{P}_2$ piecewise affine and $\mathbb{Q}_1$-iso-$\mathbb{Q}_2$ piecewise bilinear functions on $\tilde{K}$ for triangular and quadrilateral elements, respectively [33, 32]. Then let us assume that at each point of $\tilde{\Omega}$ three linearly independent unit vectors of class C^1 are prescribed $\{\boldsymbol{e}_i\}_{i=1}^3$, $\boldsymbol{e}_i \in \mathbb{R}^3$, such that $\boldsymbol{e}_1, \boldsymbol{e}_2 \perp \boldsymbol{B}$ and $\boldsymbol{e}_3 = \boldsymbol{b} \parallel \boldsymbol{B}$; such vectors can be obtained, for instance, by applying one iteration of the Gram–Schmidt orthogonalization procedure to $\{\boldsymbol{b}, \boldsymbol{e}_R, \boldsymbol{e}_z\}$ (see also § 7). Notice that it is not required that $\boldsymbol{e}_1 \perp \boldsymbol{e}_2$. Notice as well that, in general, the $\boldsymbol{e}_i$ are not induced by any coordinate system. The vector finite element space can now be defined as

$$\boldsymbol{V}_h = \left\{ \boldsymbol{v}_h \in \boldsymbol{H}^1_0(\tilde{\Omega}) \quad | \quad \boldsymbol{v}_h = v_h^1 \boldsymbol{e}_1 + v_h^2 \boldsymbol{e}_2 + v_h^{\parallel} \boldsymbol{b}, \quad v_h^1, v_h^2, v_h^{\parallel} \in V_h \right\}.$$

The main advantage of this representation is that, contrary to the standard Cartesian or cylindrical ones, it allows separating the parallel and perpendicular components of the discrete fields, letting

$$\boldsymbol{v}_h = \boldsymbol{v}_h^{\perp} + \boldsymbol{v}_h^{\parallel}, \qquad \boldsymbol{v}_h^{\perp} = v_h^1 \boldsymbol{e}_1 + v_h^2 \boldsymbol{e}_2, \quad \boldsymbol{v}_h^{\parallel} = v_h^{\parallel} \boldsymbol{b}.$$

Hence, $v_h^1 = v_h^2 = 0$ yields a purely parallel field, while $v_h^{\parallel} = 0$ yields a purely perpendicular one. Representing such fields within a standard Cartesian or cylindrical setting would not be possible, in general, because the components of the unit vectors $\boldsymbol{e}_i$ are arbitrary functions and thus the Cartesian and the cylindrical components of $\boldsymbol{v}_h^{\perp}$ and $\boldsymbol{v}_h^{\parallel}$ do not belong to any standard finite element space. Thanks to the regularity of $\boldsymbol{e}_i$, the finite element pair $\boldsymbol{V}_h, Q_h$ satisfies both hypotheses (H3) and (H4) (see [33, § 4.2.6]).

In the following, for a generic finite element space X_h, $\tilde{\mathcal{N}}_h(X_h)$ denotes the set of nodes $\tilde{\mathbf{a}}$ of X_h and $\phi_{\tilde{\mathbf{a}}}$ denotes the Lagrangian basis function associated with $\tilde{\mathbf{a}}$. The nodal degrees of freedom of $x_h \in X_h$ are indicated by $\mathtt{x}_{\tilde{\mathbf{a}}}$. The metric tensor defined by the local base is

$$g_{ij} = \boldsymbol{e}_i \cdot \boldsymbol{e}_j$$

which, taking into account the orthogonality of such vectors, can be expressed as

$$\boldsymbol{g} = \begin{bmatrix} & \boldsymbol{g}^{\perp} & 0 \\ & & 0 \\ 0 & 0 & 1 \end{bmatrix}. \tag{56}$$

The Einstein summation convention is understood for co- and contravariant indexes.

6.2 Complete space-time discretization

Having defined the finite element spaces, the spatial discretization is readily obtained from (13)–(15). Before stating it, however, it is convenient to introduce a *mass lumping* approximation for the zero-order terms. This amounts to integrating such terms with a numerical quadrature formula using the finite element nodes as quadrature nodes, i.e. we introduce

$$\int_{\tilde{\Omega}} f\, R \mathrm{d}\tilde{\boldsymbol{x}} \approx \sum_{\tilde{\mathbf{a}} \in \tilde{\mathcal{N}}_h(V_h)} w_{\tilde{\mathbf{a}}} f(\tilde{\mathbf{a}}) = I_{h,\tilde{\Omega}}(f)$$

where the quadrature weights are

$$w_{\tilde{\mathbf{a}}} = \int_{\tilde{\Omega}} \phi_{\tilde{\mathbf{a}}}\, R_{\tilde{\mathbf{a}}} \mathrm{d}\tilde{\boldsymbol{x}}.$$

The finite element discretization then reads: find $\tilde{\boldsymbol{u}}_h, \tilde{\boldsymbol{u}}_{\mathrm{e}\,h}, \tilde{\Phi}_h$ such that, for each $t \in (0, T]$, $\tilde{\boldsymbol{u}}_h, \tilde{\boldsymbol{u}}_{\mathrm{e}\,h} \in \boldsymbol{V}_h$, $\tilde{\Phi}_h \in Q_h$ and

$$\frac{\mathrm{d}}{\mathrm{d}t}(\tilde{\boldsymbol{u}}_h, \tilde{\boldsymbol{v}}_h)_{\sim,h} + \nu(\nabla\tilde{\boldsymbol{u}}_h, \nabla\tilde{\boldsymbol{v}}_h)_{\sim} - (\tilde{\Phi}_h, \nabla\cdot\tilde{\boldsymbol{v}}_h)_{\sim} - (\tilde{\boldsymbol{u}}_h \times \boldsymbol{B}, \tilde{\boldsymbol{v}}_h)_{\sim,h} = (\boldsymbol{f}, \tilde{\boldsymbol{v}}_h)_{\sim,h}, \tag{57}$$

$$\nu_{\mathrm{e}}(\nabla\tilde{\boldsymbol{u}}_{\mathrm{e}\,h}, \nabla\tilde{\boldsymbol{v}}_{\mathrm{e}\,h})_{\sim} + (\tilde{\Phi}_h, \nabla\cdot\tilde{\boldsymbol{v}}_{\mathrm{e}\,h})_{\sim} + (\tilde{\boldsymbol{u}}_{\mathrm{e}\,h} \times \boldsymbol{B}, \tilde{\boldsymbol{v}}_{\mathrm{e}\,h})_{\sim,h} = (\boldsymbol{f}_{\mathrm{e}}, \tilde{\boldsymbol{v}}_{\mathrm{e}\,h})_{\sim,h}, \tag{58}$$

$$(\nabla\cdot(\tilde{\boldsymbol{u}}_h - \tilde{\boldsymbol{u}}_{\mathrm{e}\,h}), \tilde{q}_h)_{\sim} = 0 \tag{59}$$

for all $(\tilde{\boldsymbol{v}}_h, \tilde{\boldsymbol{v}}_{\mathrm{e}\,h}, \tilde{q}_h) \in \boldsymbol{V}_h \times \boldsymbol{V}_h \times Q_h$ and with a suitable initial condition for $\tilde{\boldsymbol{u}}_h$, having defined the discrete scalar product

$$(f, g)_{\sim,h} = I_{h,\tilde{\Omega}}(fg).$$

It is now useful to compute the local matrices corresponding to (57)–(59). Besides being required for the implementation of the scheme, such matrices clarify that the projection of the vector equations

along the parallel and perpendicular directions, which is the typical starting point of the numerical discretizations for the SOL discussed in the literature, is indeed present also in our approach and corresponds to testing (57) and (58) with test functions such that $\tilde{v}_h^1 = \tilde{v}_h^2 = 0$ for the parallel direction and $\tilde{v}_h^{\parallel} = 0$ for the perpendicular one. Specifically, let us take $\tilde{\boldsymbol{v}}_h = \sum_{\tilde{\mathbf{a}} \in \tilde{\mathcal{N}}_h(\boldsymbol{V}_h)} \mathtt{v}_{\tilde{\mathbf{a}}}^i \phi_{\tilde{\mathbf{a}}} \boldsymbol{e}_i$ in (57); for the time derivative this yields

$$\frac{\mathrm{d}}{\mathrm{d}t}(\tilde{\boldsymbol{u}}_h, \tilde{\boldsymbol{v}}_h)_{\sim,h} = \sum_{\tilde{\mathbf{a}} \in \tilde{\mathcal{N}}_h(\boldsymbol{V}_h)} \mathtt{v}_{\tilde{\mathbf{a}}}^i \left[w_{\tilde{\mathbf{a}}}\, g_{ij}(\tilde{\mathbf{a}}) \right] \dot{\mathtt{u}}_{\tilde{\mathbf{a}}}^j.$$

Hence, the mass matrix is block diagonal, and by virtue of (56) each block can be further subdivided into a two-by-two block for the time derivative of $\tilde{\boldsymbol{u}}_h^{\perp}$ and a scalar equation for the time derivative of $\tilde{\boldsymbol{u}}_h^{\parallel}$. The Lorentz force term has a similar structure:

$$(\tilde{\boldsymbol{u}}_h \times \boldsymbol{B}, \tilde{\boldsymbol{v}}_h)_{\sim,h} = \sum_{\tilde{\mathbf{a}} \in \tilde{\mathcal{N}}_h(\boldsymbol{V}_h)} \mathtt{v}_{\tilde{\mathbf{a}}}^i \left[w_{\tilde{\mathbf{a}}}\, \boldsymbol{B}(\tilde{\mathbf{a}}) \left(\boldsymbol{e}_i \times \boldsymbol{e}_j \cdot \boldsymbol{b} \right) \right] \mathtt{u}_{\tilde{\mathbf{a}}}^j,$$

where $\boldsymbol{e}_i \times \boldsymbol{e}_j \cdot \boldsymbol{b}$ defines a three-by-three block with two nonvanishing entries for $(i,j) = (1,2)$ and $(i,j) = (2,1)$, which of course corresponds to the fact that the Lorentz force has no component in the parallel direction. The gradient of the electrostatic potential appears in both parallel and perpendicular directions, and couples all the vector components and the finite element nodes; in fact we have

$$(\tilde{\Phi}_h, \nabla \cdot \tilde{\boldsymbol{v}}_h)_{\sim} = \sum_{\tilde{\mathbf{a}} \in \tilde{\mathcal{N}}_h(\boldsymbol{V}_h)} \sum_{\tilde{\mathbf{d}} \in \tilde{\mathcal{N}}_h(Q_h)} \mathtt{v}_{\tilde{\mathbf{a}}}^i \left[\int_{\tilde{\Omega}} \phi_{\tilde{\mathbf{d}}} \left(\nabla \phi_{\tilde{\mathbf{a}}} \cdot \boldsymbol{e}_i + \phi_{\tilde{\mathbf{a}}} \nabla \cdot \boldsymbol{e}_i \right) R \mathrm{d}\tilde{\boldsymbol{x}} \right] \Phi_{\tilde{\mathbf{d}}}.$$

The diffusion term results in a similar matrix contribution, namely

$$\nu(\nabla \tilde{\boldsymbol{u}}_h, \nabla \tilde{\boldsymbol{v}}_h)_{\sim} = \sum_{\tilde{\mathbf{a}} \in \tilde{\mathcal{N}}_h(\boldsymbol{V}_h)} \sum_{\tilde{\mathbf{b}} \in \tilde{\mathcal{N}}_h(\boldsymbol{V}_h)} \mathtt{v}_{\tilde{\mathbf{a}}}^i \left[\nu \int_{\tilde{\Omega}} \mathcal{D}_{ij,\tilde{\mathbf{a}}\tilde{\mathbf{b}}}\, R \mathrm{d}\tilde{\boldsymbol{x}} \right] \mathtt{u}_{\tilde{\mathbf{b}}}^j$$

with

$$\mathcal{D}_{ij,\tilde{\mathbf{a}}\tilde{\mathbf{b}}} = g_{ij} \nabla \phi_{\tilde{\mathbf{a}}} \cdot \nabla \phi_{\tilde{\mathbf{b}}} + \phi_{\tilde{\mathbf{a}}} \boldsymbol{e}_j \cdot \nabla \boldsymbol{e}_i \, \nabla \phi_{\tilde{\mathbf{b}}} + \phi_{\tilde{\mathbf{b}}} \boldsymbol{e}_i \cdot \nabla \boldsymbol{e}_j \, \nabla \phi_{\tilde{\mathbf{a}}} + \phi_{\tilde{\mathbf{a}}} \phi_{\tilde{\mathbf{b}}} \nabla \boldsymbol{e}_i : \nabla \boldsymbol{e}_j.$$

The remaining terms in (58) and (59) can be expressed in terms of the same matrices derived for the first equation.

Concerning the time discretization, we follow the standard method of lines, i.e. we regard (57)–(59) as an ordinary differential equation and integrate it using a discrete time integrator. Since the $\tilde{\boldsymbol{u}}_h \times \boldsymbol{B}$ term is the stiff one, and since we are not interested in resolving the associated fast dynamics, it is natural to choose an implicit time discretization; in this work, we consider the simplest option represented by the implicit Euler method. This suppresses the fast gyration motion resulting from the $\tilde{\boldsymbol{u}}_h \times \boldsymbol{B}$ term and provides a solution where the leading order terms $-\nabla \tilde{\Phi}_h + \tilde{\boldsymbol{u}}_h \times \boldsymbol{B}$ are in very close balance. The outcome of this setting is that the *E cross B* drift velocity (8) emerges from the solution of the discretized problem rather than being postulated *a priori* in the derivation of the model equation, as it is done in the drift-reduced class of models.

This general statement can be verified by a classical dispersion analysis as follows. Let us consider for simplicity the case $\boldsymbol{B} = B_0 \boldsymbol{e}_{-\varphi}$ with $B_0 = Const$, so that the parallel velocity components can

be separated, and let us make, for the perpendicular components, the ansatz

$$\tilde{\boldsymbol{u}}^{\perp} = \hat{\tilde{\boldsymbol{u}}}^{\perp} e^{j(\tilde{\boldsymbol{k}}\cdot\tilde{\boldsymbol{x}}-\omega t)}, \qquad \tilde{\boldsymbol{u}}_{\mathrm{e}}^{\perp} = \hat{\tilde{\boldsymbol{u}}}_{\mathrm{e}}^{\perp} e^{j(\tilde{\boldsymbol{k}}\cdot\tilde{\boldsymbol{x}}-\omega t)}, \qquad \tilde{\Phi} = \hat{\tilde{\Phi}} e^{j(\tilde{\boldsymbol{k}}\cdot\tilde{\boldsymbol{x}}-\omega t)} \tag{60}$$

where $\hat{\tilde{\boldsymbol{u}}}^{\perp}, \hat{\tilde{\boldsymbol{u}}}_{\mathrm{e}}^{\perp}, \hat{\tilde{\Phi}}$ are constants and $j = \sqrt{-1}$. Let us start from the continuous problem: substituting (60) into (5)–(7) and taking $\boldsymbol{f} = \boldsymbol{f}_{\mathrm{e}} = 0$ we arrive at a homogeneous system which admits a nontrivial solution if the matrix determinant vanishes, i.e.

$$k^2 \left(a\omega^2 + b\omega + c\right) = 0, \tag{61}$$

with $k^2 = |\tilde{\boldsymbol{k}}|^2$ and

$$a = -\nu_{\mathrm{e}} k^2, \qquad b = -j\left(B_0^2 + \nu_{\mathrm{e}}(2\nu + \nu_{\mathrm{e}})k^4\right), \qquad c = (\nu + \nu_{\mathrm{e}})(B_0^2 + \nu\nu_{\mathrm{e}}k^4)k^2.$$

Notice that, for the second order term in ω,

$$\Delta = b^2 - 4ac = -(B_0^2 - \nu_{\mathrm{e}}^2 k^4)^2 < 0.$$

This indicates the existence of three modes:

- $\tilde{\boldsymbol{k}} = 0$ is a uniform mode with $\omega_1 = \pm B_0$, $\hat{\tilde{\boldsymbol{u}}}^{\perp} \neq 0$, $\hat{\tilde{\boldsymbol{u}}}_{\mathrm{e}}^{\perp} = 0$ and $\hat{\tilde{\Phi}} = Const$;
- $\omega_2 = \frac{-b-\sqrt{\Delta}}{2a} = -j(\nu + \nu_{\mathrm{e}})k^2$ implies $\hat{\tilde{\boldsymbol{u}}}^{\perp} = \hat{\tilde{\boldsymbol{u}}}_{\mathrm{e}}^{\perp} = \frac{B_0 \boldsymbol{b}\times + \nu_{\mathrm{e}} k^2}{B_0^2 + \nu_{\mathrm{e}}^2 k^4} j\tilde{\boldsymbol{k}}\hat{\tilde{\Phi}}$;
- $\omega_3 = \frac{-b+\sqrt{\Delta}}{2a} = -j\left(\frac{B_0^2}{\nu_{\mathrm{e}} k^2} + \nu k^2\right)$ implies $\hat{\tilde{\boldsymbol{u}}}^{\perp} = \frac{\nu_{\mathrm{e}} k^2}{B_0} \frac{B_0 + \nu_{\mathrm{e}} k^2 \boldsymbol{b}\times}{B_0^2 + \nu_{\mathrm{e}}^2 k^4} j\tilde{\boldsymbol{k}}\hat{\tilde{\Phi}}$, $\hat{\tilde{\boldsymbol{u}}}_{\mathrm{e}}^{\perp} = \frac{B_0 \boldsymbol{b}\times + \nu_{\mathrm{e}} k^2}{B_0^2 + \nu_{\mathrm{e}}^2 k^4} j\tilde{\boldsymbol{k}}\hat{\tilde{\Phi}}$.

The first mode exhibits the fast gyration and no attenuation, the second mode is dominated by the *E cross B* drift and decays slowly due to the effect of the viscosity and the third mode is a rapidly decaying mode. Considering now the semi discretized problem, the analysis proceeds along the same lines and (61) is still valid provided that ω is substituted with

$$\omega_{\mathrm{IE}} = -\frac{1 - e^{j\omega\Delta t}}{j\Delta t},$$

where Δt is the time step. The first mode is still characterized by $\tilde{\boldsymbol{k}} = 0$, $\omega_{\mathrm{IE}} = \pm B_0$, resulting in the complex frequency $\omega = \mathrm{Re}(\omega) + j\mathrm{Im}(\omega)$ with

$$\mathrm{Re}(\omega) = \pm\frac{1}{\Delta t}\mathrm{atan}(B_0\Delta t), \qquad \mathrm{Im}(\omega) = -\frac{1}{2\Delta t}\log(1 + B_0^2\Delta t^2),$$

so that it is numerically damped. The remaining two modes have then the same structure as in the continuous case and a purely decaying behaviour.

6.3 Iterative solution of the linear system

The discretized problem illustrated in section 6.2 leads to a linear system coupling two vector unknown, namely $\tilde{\boldsymbol{u}}_h$ and $\tilde{\boldsymbol{u}}_{\mathrm{e}\,h}$, and one scalar unknown, namely $\tilde{\Phi}_h$. It is highly desirable to avoid solving this system with a fully coupled approach (also called "monolithic" approach), which would result in a very large, indefinite matrix. Moreover, a fully coupled approach would not scale when

considering multiple ion species, as it is required for practical applications, since each ion species introduces an additional vector unknown in the problem. The goal of this section is to discuss how it is possible to solve separate linear systems for the electric potential and each vector unknown using a variation of the classical Uzawa algorithm for the Stokes problem [34, 35, 36, 33].

Discretizing (57)–(59) with the implicit Euler scheme results in the linear system

$$a(\tilde{\boldsymbol{u}}_h^{n+1}, \tilde{\boldsymbol{v}}_h) + b(\tilde{\boldsymbol{v}}_h, \tilde{\Phi}_h^{n+1}) = f(\tilde{\boldsymbol{v}}_h), \tag{62}$$

$$a_{\mathrm{e}}(\tilde{\boldsymbol{u}}_{\mathrm{e}\,h}^{n+1}, \tilde{\boldsymbol{v}}_{\mathrm{e}\,h}) - b(\tilde{\boldsymbol{v}}_{\mathrm{e}\,h}, \tilde{\Phi}_h^{n+1}) = f_{\mathrm{e}}(\tilde{\boldsymbol{v}}_{\mathrm{e}\,h}), \tag{63}$$

$$b(\tilde{\boldsymbol{u}}_h^{n+1} - \tilde{\boldsymbol{u}}_{\mathrm{e}\,h}^{n+1}, \tilde{q}_h) = 0 \tag{64}$$

where

$$\begin{aligned} a(\tilde{\boldsymbol{u}}_h, \tilde{\boldsymbol{v}}_h) &= \frac{1}{\Delta t}(\tilde{\boldsymbol{u}}_h, \tilde{\boldsymbol{v}}_h)_{\sim,h} + \nu(\nabla\tilde{\boldsymbol{u}}_h, \nabla\tilde{\boldsymbol{v}}_h)_{\sim} - (\tilde{\boldsymbol{u}}_h \times \boldsymbol{B}, \tilde{\boldsymbol{v}}_h)_{\sim,h}, \\ a_{\mathrm{e}}(\tilde{\boldsymbol{u}}_{\mathrm{e}\,h}, \tilde{\boldsymbol{v}}_{\mathrm{e}\,h}) &= \nu_{\mathrm{e}}(\nabla\tilde{\boldsymbol{u}}_{\mathrm{e}\,h}, \nabla\tilde{\boldsymbol{v}}_{\mathrm{e}\,h})_{\sim} + (\tilde{\boldsymbol{u}}_{\mathrm{e}\,h} \times \boldsymbol{B}, \tilde{\boldsymbol{v}}_h)_{\sim,h}, \\ b(\tilde{\boldsymbol{v}}_h, \tilde{q}_h) &= -(\nabla \cdot \tilde{\boldsymbol{v}}_h, \tilde{q}_h)_{\sim} \end{aligned}$$

and

$$f(\tilde{\boldsymbol{v}}_h) = \frac{1}{\Delta t}(\tilde{\boldsymbol{u}}_h^n, \tilde{\boldsymbol{v}}_h)_{\sim,h} + (\boldsymbol{f}, \tilde{\boldsymbol{v}}_h)_{\sim,h}, \qquad f_{\mathrm{e}}(\tilde{\boldsymbol{v}}_{\mathrm{e}\,h}) = (\boldsymbol{f}_{\mathrm{e}}, \tilde{\boldsymbol{v}}_{\mathrm{e}\,h})_{\sim,h}.$$

Define now $\tilde{\boldsymbol{u}}_h^{\boldsymbol{f}}, \tilde{\boldsymbol{u}}_{\mathrm{e}\,h}^{\boldsymbol{f}_{\mathrm{e}}} \in \boldsymbol{V}_h$ by

$$a(\tilde{\boldsymbol{u}}_h^{\boldsymbol{f}}, \tilde{\boldsymbol{v}}_h) = f(\tilde{\boldsymbol{v}}_h), \qquad a_{\mathrm{e}}(\tilde{\boldsymbol{u}}_{\mathrm{e}\,h}^{\boldsymbol{f}_{\mathrm{e}}}, \tilde{\boldsymbol{v}}_{\mathrm{e}\,h}) = f_{\mathrm{e}}(\tilde{\boldsymbol{v}}_{\mathrm{e}\,h})$$

as well as two linear operators $\boldsymbol{U}, \boldsymbol{U}_{\mathrm{e}} : Q_h \to \boldsymbol{V}_h$ such that, for $\tilde{q}_h \in Q_h$,

$$a(\boldsymbol{U}\tilde{q}_h, \tilde{\boldsymbol{v}}_h) = -b(\tilde{\boldsymbol{v}}_h, \tilde{q}_h), \qquad a_{\mathrm{e}}(\boldsymbol{U}_{\mathrm{e}}\tilde{q}_h, \tilde{\boldsymbol{v}}_{\mathrm{e}\,h}) = b(\tilde{\boldsymbol{v}}_{\mathrm{e}\,h}, \tilde{q}_h) \tag{65}$$

for every $\tilde{\boldsymbol{v}}_h, \tilde{\boldsymbol{v}}_{\mathrm{e}\,h} \in \boldsymbol{V}_h$ (such operators are well defined since both a and a_{e} are positive definite). The solution of (62)–(64) is uniquely characterized by

$$-b(\boldsymbol{U}\tilde{\Phi}_h^{n+1} - \boldsymbol{U}_{\mathrm{e}}\tilde{\Phi}_h^{n+1}, \tilde{q}_h) = b(\tilde{\boldsymbol{u}}_h^{\boldsymbol{f}} - \tilde{\boldsymbol{u}}_{\mathrm{e}\,h}^{\boldsymbol{f}_{\mathrm{e}}}, \tilde{q}_h) \tag{66}$$

for every $\tilde{q}_h \in Q_h$; the main idea is to apply an iterative algorithm for such a problem.

It can be verified that the left-hand-side of (66) defines a positive definite operator, which however is not symmetric. Indeed, for $\tilde{p}_h, \tilde{q}_h \in Q_h$, we have

$$-b(\boldsymbol{U}\tilde{p}_h - \boldsymbol{U}_{\mathrm{e}}\tilde{p}_h, \tilde{q}_h) = a(\boldsymbol{U}\tilde{q}_h, \boldsymbol{U}\tilde{p}_h) + a_{\mathrm{e}}(\boldsymbol{U}_{\mathrm{e}}\tilde{q}_h, \boldsymbol{U}_{\mathrm{e}}\tilde{p}_h).$$

For this reason, the GMRES method [37] is used to solve (66). To summarize the resulting procedure, let us first rewrite (65) and (66) in matrix form as

$$A\mathtt{U}_q = -B^T\mathtt{q}, \qquad A_{\mathrm{e}}\mathtt{U}_{\mathrm{e}\,q} = B^T\mathtt{q} \tag{67}$$

and

$$B(A^{-1} + A_{\mathrm{e}}^{-1})B^T\Phi = B(\mathtt{u}^{\boldsymbol{f}} - \mathtt{u}_{\mathrm{e}}^{\boldsymbol{f}_{\mathrm{e}}}), \tag{68}$$

where $\mathtt{q}, \mathtt{U}_q, \mathtt{U}_{\mathrm{e}\,q}$ are the arrays of the nodal degrees of freedom of $\tilde{q}_h, \boldsymbol{U}\tilde{q}_h, \boldsymbol{U}_{\mathrm{e}}\tilde{q}_h$ and $\Phi, \mathtt{u}^{\boldsymbol{f}}, \mathtt{u}_{\mathrm{e}}^{\boldsymbol{f}_{\mathrm{e}}}$ those of $\tilde{\Phi}_h^{n+1}, \tilde{\boldsymbol{u}}_h^{\boldsymbol{f}}, \tilde{\boldsymbol{u}}_{\mathrm{e}\,h}^{\boldsymbol{f}_{\mathrm{e}}}$. The matrix-free versions of the GMRES solver relies on two methods to compute,

given an arbitrary $\Phi^{(k)}$, the matrix-vector product and the residual of (68). Concerning the matrix-vector product, we have

$$B(A^{-1} + A_{\mathrm{e}}^{-1})B^T\Phi^{(k)} = -B(\mathtt{U}_{\Phi^{(k)}} - \mathtt{U}_{\mathrm{e}\,\Phi^{(k)}}), \tag{69}$$

resulting in the following steps:

- compute $\mathtt{U}_{\Phi^{(k)}}, \mathtt{U}_{\mathrm{e}\,\Phi^{(k)}}$ solving (67) for $\mathtt{q} = \Phi^{(k)}$ with a direct method
- evaluate the right-hand-side of (69) substituting the corresponding finite element functions in $-b(\boldsymbol{U}\tilde{\Phi}_h^{(k)} - \boldsymbol{U}_{\mathrm{e}}\tilde{\Phi}_h^{(k)}, \tilde{q}_h)$.

Concerning the residual, we have

$$B(\mathtt{u}^{\boldsymbol{f}} - \mathtt{u}_{\mathrm{e}}^{\boldsymbol{f}_{\mathrm{e}}}) - B(A^{-1} + A_{\mathrm{e}}^{-1})B^T\Phi^{(k)} = B((\mathtt{u}^{\boldsymbol{f}} + \mathtt{U}_{\Phi^{(k)}}) - (\mathtt{u}_{\mathrm{e}}^{\boldsymbol{f}_{\mathrm{e}}} + \mathtt{U}_{\mathrm{e}\,\Phi^{(k)}})), \tag{70}$$

resulting in the following steps:

- compute $\mathtt{u}^{\boldsymbol{f}} + \mathtt{U}_{\Phi^{(k)}} = A^{-1}(\mathtt{f} - B^T\Phi^{(k)})$ as well as $\mathtt{u}_{\mathrm{e}}^{\boldsymbol{f}_{\mathrm{e}}} + \mathtt{U}_{\mathrm{e}\,\Phi^{(k)}} = A_{\mathrm{e}}^{-1}(\mathtt{f}_{\mathrm{e}} + B^T\Phi^{(k)})$ with a direct method
- evaluate the right-hand-side of (70) substituting the corresponding finite element functions in $b((\tilde{\boldsymbol{u}}_h^{\boldsymbol{f}} + \boldsymbol{U}\tilde{\Phi}_h^{(k)}) - (\tilde{\boldsymbol{u}}_{\mathrm{e}\,h}^{\boldsymbol{f}_{\mathrm{e}}} + \boldsymbol{U}_{\mathrm{e}}\tilde{\Phi}_h^{(k)}), \tilde{q}_h)$.

Remark 1. *The proposed algorithm requires a direct method for the solution of (67). This seems a viable option for the considered problem, since these linear systems, which correspond to two-dimensional problems, are not expected to be extremely large. At the same time, this algorithm scales well in presence of multiple ion species, since each ion species would result in a separate linear system. However, if one wants to adopt an iterative solver also for (67), adopting an inexact Uzawa scheme, the methods proposed in [36] can be considered.*

Remark 2. *To leading order, the two operators $\boldsymbol{U}, \boldsymbol{U}_{\mathrm{e}}$ yield the* E cross B *drift velocity (8), i.e.*

$$\boldsymbol{U}\tilde{\Phi}_h \approx \boldsymbol{U}_{\mathrm{e}}\tilde{\Phi}_h \approx \frac{-\nabla\tilde{\Phi}_h \times \boldsymbol{B}}{B^2}.$$

This term, being ambipolar, does not contribute to the current $\boldsymbol{U}\tilde{\Phi}_h - \boldsymbol{U}_{\mathrm{e}}\tilde{\Phi}_h$ appearing in (66). So, the presence of the ion inertia and of the diffusion terms, despite contributing only a small perturbation to the operators $\boldsymbol{U}, \boldsymbol{U}_{\mathrm{e}}$, is essential in determining their difference, and thus the solution of (66).

6.3.1 Left-preconditioned GMRES iterations

To improve the convergence of the GMRES iterations, a preconditioned version of the algorithm can be considered. In this work, we restrict ourselves to a simple left-preconditioned version of (68), where both sides of the equation are multiplied by

$$P \approx B(A^{-1} + A_{\mathrm{e}}^{-1})B^T.$$

The matrix P is constructed as

$$P = B(A_0^{-1} + A_{0,\mathrm{e}}^{-1})B^T,$$

where A_0 and $A_{0,\mathrm{e}}$ include only the 3×3 diagonal blocks of A and A_e, respectively. Due to the lumping of the mass matrix and the Lorentz force terms, this implies that the only difference between P and the complete matrix of (68) is due to the diffusion terms. It can be verified that P is a positive definite matrix, and since its dimension is $\dim(Q_h)$ and it is sparse it can be computed explicitly and a direct solver can be used for the associated linear system.

7 Numerical experiments

To test the proposed numerical scheme, we consider in this section two cases: the first one involves simplified geometry and coefficients and has a known analytic solution, which allows us to perform a convergence test, while the second one uses a more realistic set-up, including an X point.

Following a standard representation (see Eq. (6.2.13) in [3]), the magnetic field is prescribed as

$$\boldsymbol{B} = \frac{1}{R}\left(I\boldsymbol{e}_{-\varphi} + \nabla\psi \times \boldsymbol{e}_{-\varphi}\right),$$

where $I = B_0 R_0$ is a constant and $\psi = \psi(R, z)$. This representation separates the toroidal and the poloidal components of $\boldsymbol{B}$; it also provides an immediate expression for the flux surfaces and the poloidal flux, namely $\psi = Const$ and $\Psi_{\mathrm{pol}} = 2\pi\psi$. The computational grids are built so that, on most of the domain, they are aligned in the sense of [10], which can be rephrased for both triangular and quadrilateral elements as follows: if a contour line $c = \{\tilde{\boldsymbol{x}} \in \tilde{\Omega} \mid \psi(\tilde{\boldsymbol{x}}) = Const\}$ passes through a vertex of $\tilde{\mathcal{T}}_h$, then for each element $\tilde{K}$ connected to that vertex either the intersection with c reduces to the vertex itself, or one side of $\tilde{K}$ has both vertexes belonging to c. The alignment, however, can be violated in selected regions where it would result in a too strong constraint, such as close to the domain boundaries, around the X point or in transition regions around patches of local refinement. Examples of such grids are shown in Figures 3 and 4. Concerning the choice of $\{\boldsymbol{e}_i\}_{i=1}^3$, as noted in § 6.1 we have $\boldsymbol{e}_3 = \boldsymbol{b}$ while there is freedom in the choice of $\boldsymbol{e}_1$ and $\boldsymbol{e}_2$. We take

$$\boldsymbol{e}_1 = \widehat{(\mathcal{I} - \boldsymbol{b}\otimes\boldsymbol{b})\boldsymbol{e}_R}, \qquad \boldsymbol{e}_2 = \widehat{(\mathcal{I} - \boldsymbol{b}\otimes\boldsymbol{b})\boldsymbol{e}_z},$$

where $\widehat{\cdot}$ denotes normalization. An alternative choice would be substituting $\boldsymbol{e}_R$ and $\boldsymbol{e}_z$ in the above expression with $\nabla\psi$ and $\boldsymbol{e}_{-\varphi} \times \nabla\psi$ (at least where $\nabla\psi$ does not vanish), yielding a radial and poloidal decomposition analogous to [12]. Notice that $\boldsymbol{e}_1$ and $\boldsymbol{e}_2$ do not need to be mutually orthogonal.

7.1 Convergence test

We consider $\tilde{\Omega} = (R_0 - a, R_0 + a) \times (-a, a)$ and

$$I = B_0 R_0, \qquad \psi = a R_0 B_p \frac{(R - R_0)^2 + z^2}{2a^2};$$

the resulting magnetic field has an O point at $(R_0, 0)$, closed magnetic surfaces for $(R-R_0)^2+z^2 < a^2$ and open magnetic surfaces for $(R - R_0)^2 + z^2 > a^2$. The forcing terms are $\boldsymbol{f} = \nu\boldsymbol{\varpi}$ and $\boldsymbol{f}_\mathrm{e} = \nu_\mathrm{e}\boldsymbol{\varpi}$, with

$$\boldsymbol{\varpi} = \left[0, \alpha\frac{R_0 - 4R}{aR_0R} - \beta\frac{B_p}{B_0}\frac{R_0^2}{aR^3}, 0\right]^T,$$

and constant in time, nonhomogeneous Dirichlet boundary conditions for $\boldsymbol{u}, \boldsymbol{u}_{\mathrm{e}}$ are enforced so that, after an initial transient, the analytic steady state solution is

$$\tilde{\boldsymbol{u}} = \tilde{\boldsymbol{u}}_{\mathrm{e}} = \alpha \frac{R}{aR_0} \begin{bmatrix} -z \\ R - R_0 \\ 0 \end{bmatrix} + \beta \frac{B_p}{B_0} \frac{R_0}{aR} \begin{bmatrix} z \\ -(R - R_0) \\ \frac{B_0}{B_p} a \end{bmatrix}$$

and

$$\tilde{\Phi} = \frac{1}{2} a B_0 \alpha \left(\frac{(R - R_0)^2 + z^2}{a^2} - \frac{2}{3} \right).$$

The numerical values of the coefficients are $R_0 = 2$, $a = 1$, $B_0 = 10$, $B_p = 12.5$, $\nu = 1$, $\nu_{\mathrm{e}} = 0.01$, $\alpha = 0.1$ and $\beta = 1$.

Six unstructured grids are considered, halving the mesh size h, two of which are shown in Figure 3. It can be observed that most of the elements are aligned to the $\psi = Const$ circular

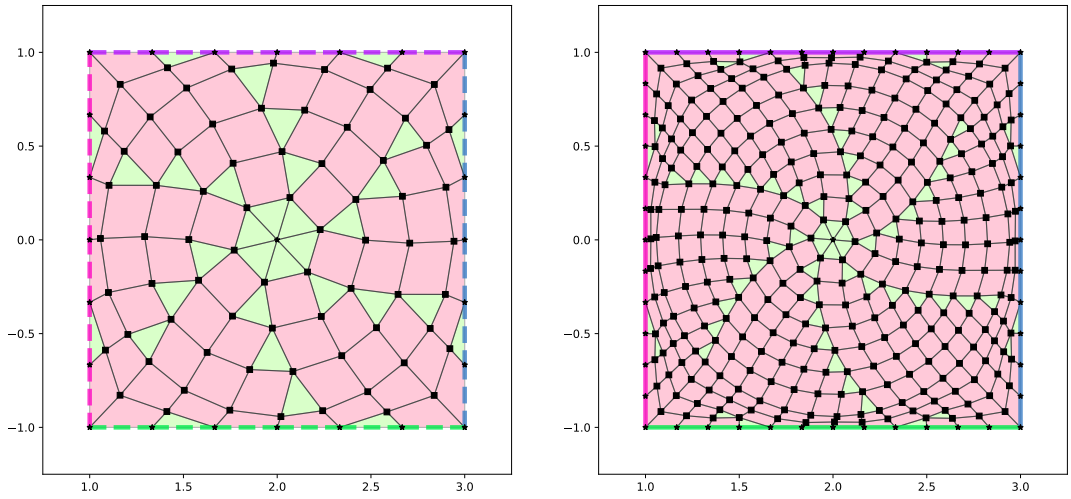

Figure 3: Unstructured grids for the convergence test using 32 triangles and 68 quadrilaterals (left) and 64 triangles and 304 quadrilaterals (right). The number of degrees of freedom of Q_h in the two cases is 97 and 361.

contours, while such alignment is not respected in the four corners, where it would lead to very distorted elements. Also, mixing triangular and quadrilateral elements allows to achieve a good overall regularity of the grid.

The numerical computations are performed until $T = 4000$, which is much larger than the relaxation time of the system, using the implicit Euler scheme with time-step $\Delta t = 1$, and the resulting numerical solution is compared to the steady state analytic solution. To avoid errors associated with the inexact solution of the linear problem, a directed solver is used for the complete linear system (62)–(64). The resulting error norms are shown in Tables 2 and 3, where the expected second order convergence can be observed. Similar results, not included here, have been observed

Table 2: Computed error norms for the electrostatic potential $\tilde{\Phi} - \tilde{\Phi}_h$. The numerical convergence rates are also reported.

$\dim(Q_h)$	$\|\tilde{\Phi} - \tilde{\Phi}_h\|_{L^2}$	
31	$4.2 \cdot 10^{-2}$	–
97	$1.1 \cdot 10^{-2}$	1.98
361	$2.8 \cdot 10^{-3}$	1.92
1393	$7.2 \cdot 10^{-4}$	1.97
5473	$1.8 \cdot 10^{-4}$	2.00
21697	$4.5 \cdot 10^{-5}$	2.00

Table 3: Computed error norms $\tilde{\boldsymbol{u}} - \tilde{\boldsymbol{u}}_h$ and $\tilde{\boldsymbol{u}}_\mathrm{e} - \tilde{\boldsymbol{u}}_{\mathrm{e}\,h}$. The numerical convergence rates are also reported.

$\dim(V_h)$	$\|\tilde{\boldsymbol{u}} - \tilde{\boldsymbol{u}}_h\|_{\boldsymbol{L}^2}$		$\|\tilde{\boldsymbol{u}}_\mathrm{e} - \tilde{\boldsymbol{u}}_{\mathrm{e}\,h}\|_{\boldsymbol{L}^2}$		$\|\tilde{\boldsymbol{u}} - \tilde{\boldsymbol{u}}_h\|_{\boldsymbol{H}^1}$		$\|\tilde{\boldsymbol{u}}_\mathrm{e} - \tilde{\boldsymbol{u}}_{\mathrm{e}\,h}\|_{\boldsymbol{H}^1}$	
109	$2.8 \cdot 10^{-2}$	–	$7.4 \cdot 10^{-2}$	–	$5.6 \cdot 10^{-1}$	–	$9.5 \cdot 10^{-1}$	–
361	$7.1 \cdot 10^{-3}$	2.0	$1.1 \cdot 10^{-2}$	2.8	$2.9 \cdot 10^{-1}$	1.0	$3.4 \cdot 10^{-1}$	1.5
1393	$1.8 \cdot 10^{-3}$	2.0	$2.2 \cdot 10^{-3}$	2.3	$1.4 \cdot 10^{-1}$	1.0	$1.5 \cdot 10^{-1}$	1.1
5473	$4.5 \cdot 10^{-4}$	2.0	$5.0 \cdot 10^{-4}$	2.2	$7.1 \cdot 10^{-2}$	1.0	$7.3 \cdot 10^{-2}$	1.1
21697	$1.1 \cdot 10^{-4}$	2.0	$1.2 \cdot 10^{-4}$	2.1	$3.6 \cdot 10^{-2}$	1.0	$3.6 \cdot 10^{-2}$	1.0
86401	$2.8 \cdot 10^{-5}$	2.0	$3.0 \cdot 10^{-5}$	2.0	$1.8 \cdot 10^{-2}$	1.0	$1.8 \cdot 10^{-2}$	1.0

using structured grids composed entirely of quadrilaterals or triangular elements. This is expected, since in this case the solution is very smooth. Indeed, the use of unstructured, aligned grids for this test is motivated by testing the numerical formulation in the most general case, rather than by the strong anisotropy of the solution.

7.2 Test with a more realistic geometry

In this case, we consider the domain $\tilde{\Omega}$ depicted in Figure 4, left, which includes all the main components illustrated by the schematic representation of Figure 2, right, namely: a separatrix with an X point, closed and open field lines, a wall and two divertor plates. The central region, containing the plasma core, has been omitted, mimicking what is typically done for SOL computations. The magnetic field is specified by

$$I = B_0 R_0, \qquad \psi = a R_0 B_p \left(\frac{(R - R_0)^2 + z^2}{2a^2} - \frac{z^3}{3a^2 z_0} \right),$$

while no forcing terms are present: $\boldsymbol{f} = \boldsymbol{f}_\mathrm{e} = 0$. Homogeneous Dirichlet boundary conditions are enforced for $\boldsymbol{u}$ and $\boldsymbol{u}_\mathrm{e}$ on most of the domain boundary with the following exceptions: on the boundary towards the plasma core we set $\tilde{\boldsymbol{u}} = \tilde{\boldsymbol{u}}_\mathrm{e} = 0.1[R - R_0, z, 0]^T$, on the left divertor plate we set $\tilde{\boldsymbol{u}} = \tilde{\boldsymbol{u}}_\mathrm{e} = 0.1[-2, -1, 0]$ and on the right divertor plate we set $\tilde{\boldsymbol{u}} = \tilde{\boldsymbol{u}}_\mathrm{e} = 0.1[-2, 1, 0]$. The numerical values of the coefficients are $R_0 = 165$, $a = 60$, $z_0 = -90$, $B_0 = 2.5 \cdot 10^4$, $B_p = 0.2 B_0$,

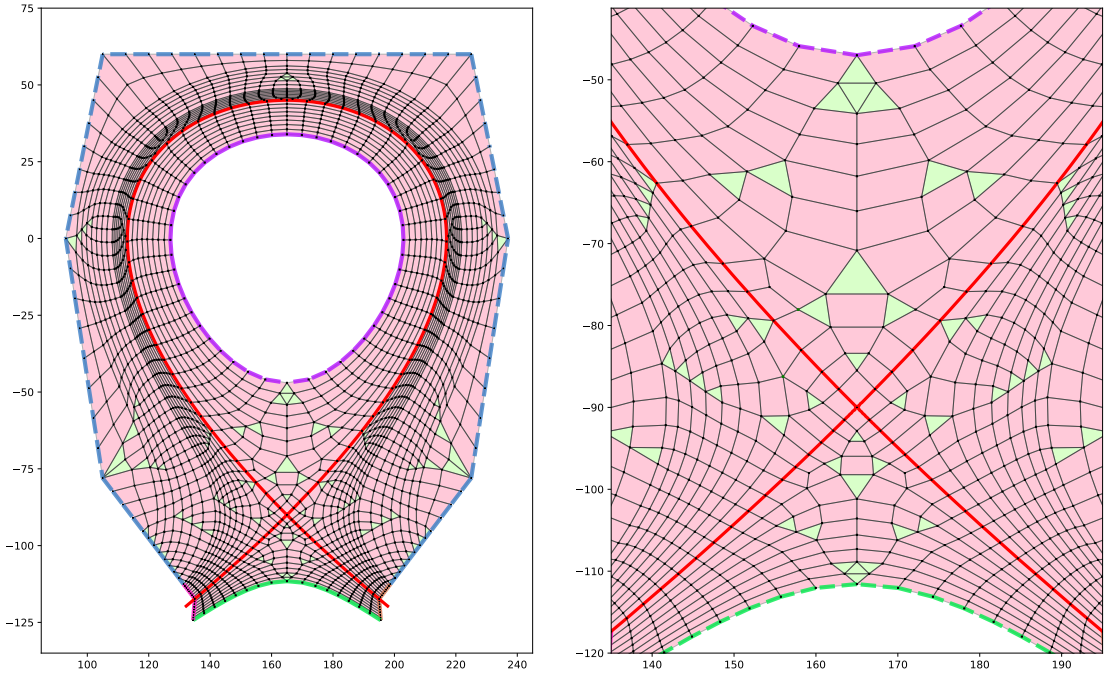

Figure 4: Domain $\tilde{\Omega}$ including a plasma facing wall (blue), left and right divertor plates (magenta and brown) and a private region (green). The plasma core has been excluded from the computational domain, resulting in an additional boundary (purple). The separatrix is marked in red. The whole grid (left) is composed of 120 triangular and 2068 quadrilateral elements; a detail view of the X point is also shown (right).

$\nu = 10^5$, $\nu_\mathrm{e} = 10^2$. We stress the fact that, on the one hand, these values, as well as the results of this test, should not be directly compared with those encountered in simulation of real devices, since our model lacks anyway various physically relevant terms; on the other hand, however, these coefficients are chosen in order to test those aspects of our model which do appear in real devices, namely a) the fact that the ion viscosity is larger than the electron one and b) the fact that the Lorentz force term is dominant, except for some thin boundary layers where, due to the presence of strong gradients, it is balanced by the viscous term. The first condition is motivated by the standard Braginskii expression for the viscosity coefficients. In fact, if one considers the viscosity coefficients denoted by η_0^i and η_0^e in [2] as order-of-magnitude estimates for our isotropic coefficients, ν and ν_e, respectively, then

$$\nu \approx \eta_0^\mathrm{i} = 0.96 n k_B T_\mathrm{i} \tau_\mathrm{i},$$
$$\nu_\mathrm{e} \approx \eta_0^\mathrm{e} = 0.73 n k_B T_\mathrm{e} \tau_\mathrm{e},$$

where τ_i and τ_e are the ion and electron collision time, respectively (see [2] for the precise definition), $n = n_\mathrm{i} = n_\mathrm{e}$ is the number density for a quasi-neutral Hydrogen plasma, T_e is the electron

temperature and T_i is the ion temperature. Under the assumption that the temperature ratio $T_\mathrm{e}/T_\mathrm{i}$ is of the order of unity, one finds

$$\nu_\mathrm{e}/\nu \approx \tau_\mathrm{e}/\tau_\mathrm{i} \approx \sqrt{m_\mathrm{e}/m_\mathrm{i}},$$

which shows that the electron viscosity is smaller than the ion viscosity by a square root of the mass ratio which is $\approx 2.3 \times 10^{-2}$. The second condition can be verified estimating the width of the boundary layers as follows: to balance the Lorentz force term, the viscous term requires variations of the velocity over a length scale ϵ_ν such that

$$\nu \epsilon_\nu^{-2} = B_0.$$

Given the above coefficients, this implies $\epsilon_\nu = 1$, $\epsilon_{\nu_\mathrm{e}} = 0.063$, which are much smaller than $\tilde{\Omega}$.

Two different grids are considered, obtained refining uniformly the grid shown in Figure 4 once and twice, respectively. The resulting numbers of degrees of freedom are $\dim(V_h) = 34384$, $\dim(Q_h) = 8680$ and $\dim(V_h) = 136864$, $\dim(Q_h) = 34384$. Such grids are aligned in most of the domain and are nearly structured around the separatrix, where quadrilateral elements allow good regularity and higher resolution in the radial direction. Few triangular elements are inserted to obtain a uniform resolution on each flux surface; moreover unstructured, not aligned patches are used to resolve the X point and close to the domain boundary.

Computations are carried out starting from $\tilde{\boldsymbol{u}} = \tilde{\boldsymbol{u}}_\mathrm{e} = 0$ and $\Phi = 0$ until $T = 0.01$, a time after which no significant changes are observed. For these tests, a directed solver is used for the complete linear system (62)–(64). The time-step is $\Delta t = 6.25 \cdot 10^{-5}$. The time evolution of the L^2 norms of the numerical solution is shown in Figure 5 for the coarsest grid. For the same computation,

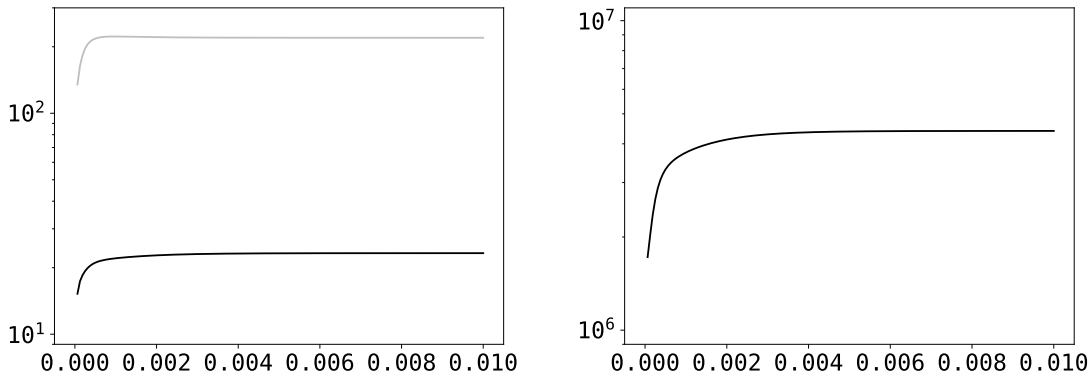

Figure 5: Left: time evolution of $\|\tilde{\boldsymbol{u}}\|_{\boldsymbol{L}^2}$ (black) and $\|\tilde{\boldsymbol{u}}_\mathrm{e}\|_{\boldsymbol{L}^2}$ (gray). Right: time evolution of $\|\tilde{\Phi}\|_{L^2}$.

Figure 6 shows the toroidal component of the ion and electron velocities $\tilde{\boldsymbol{u}} \cdot \boldsymbol{e}_{-\varphi}$ and $\tilde{\boldsymbol{u}}_\mathrm{e} \cdot \boldsymbol{e}_{-\varphi}$. It can be seen that such components do not vanish, despite the absence of toroidal components both in the boundary conditions and in the forcing terms. This is indeed a consequence of $B_p \neq 0$, which couples the toroidal velocity components with the forcing terms in the poloidal plane. The corresponding electrostatic potential is shown in Figure 7, left. Here, it can be seen that the $\tilde{\Phi} = Const$ contours

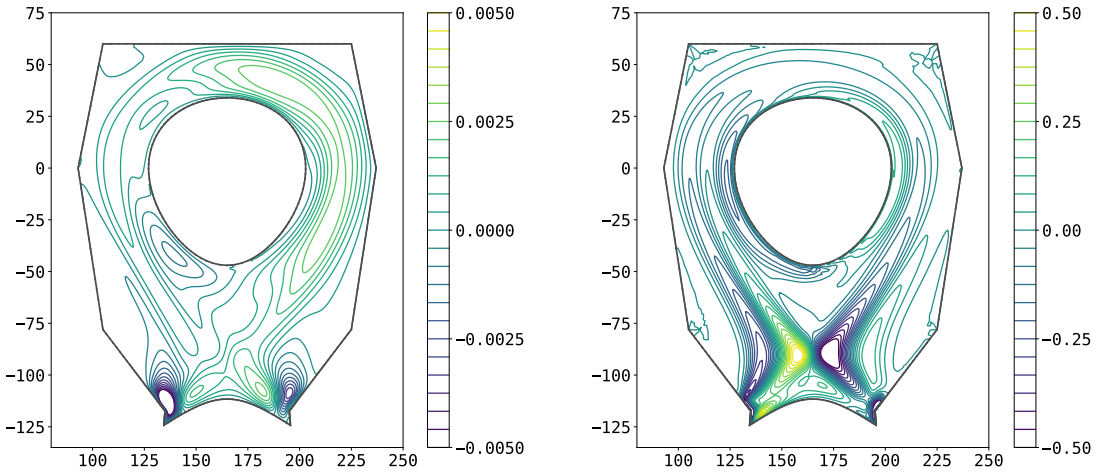

Figure 6: Toroidal velocity components at $t = T$ for $\dim(V_h) = 34384$, $\dim(Q_h) = 8680$: $\tilde{\boldsymbol{u}} \cdot \boldsymbol{e}_{-\varphi}$, left, and $\tilde{\boldsymbol{u}}_{\mathrm{e}} \cdot \boldsymbol{e}_{-\varphi}$, right. Notice that the two plots use different color scales.

tend to coincide with the magnetic surfaces. This is a consequence of the parallel velocity equation for the electrons, as noted in § 2. An analogous result is obtained using the more refined grid, as shown in Figure 7, right. For this second computation, we also plot the parallel and perpendicular gradients of the electrostatic potential in Figure 8 and the perpendicular ion and electron velocities in Figure 9. The profiles of $(\nabla\Phi)^{\parallel}$ and $(\nabla\Phi)^{\perp}$ show that, away from the boundary layers, a large gradient of the electrostatic potential can only be sustained in the perpendicular direction, where it is balanced by the Lorentz force, while the profiles of $\tilde{\boldsymbol{u}}^{\perp}$, $\tilde{\boldsymbol{u}}_{\mathrm{e}}^{\perp}$ and $\tilde{\boldsymbol{u}}^{\perp} - \tilde{\boldsymbol{u}}_{\mathrm{e}}^{\perp}$ indicate that, away from the boundary layers, $\tilde{\boldsymbol{u}}^{\perp} \approx \tilde{\boldsymbol{u}}_{\mathrm{e}}^{\perp}$. These results are in good agreement with (8). Finally, the importance of using a stable finite element pair for $\boldsymbol{V}_h$ and Q_h is verified repeating the computations with $V_h = Q_h$ and reporting the computed electrostatic potential in Figure 10. Here, it can be seen that the unstable pair results in severe grid-scale oscillations in $\tilde{\Phi}$, which can not be cured by refining the computational grid.

7.3 Iterative solution of the linear system

To test the iterative solution strategy discussed in § 6.3, we consider now a single time-step from $t_a = 1.25 \cdot 10^{-4}$ to $t_b = 1.875 \cdot 10^{-4}$ of the coarse grid computation of § 7.2 and solve it iteratively using the solution at t_a as initial guess for the linear iterations. This specific time-step is chosen since the solution has not reached the steady state condition. Figure 11 shows the residual of the linear iterations, together with the L^2 error norms of the ion and electron velocities and of the electrostatic potential, computed using the solution of the monolithic approach as a reference. All the values are normalized with the respective values for the initial iterations so that the four curves start from 1. It can be seen that the plane GMRES iteration indeed do result in a convergent algorithm, the convergence rate however is slow for the first 300 iterations. The preconditioned

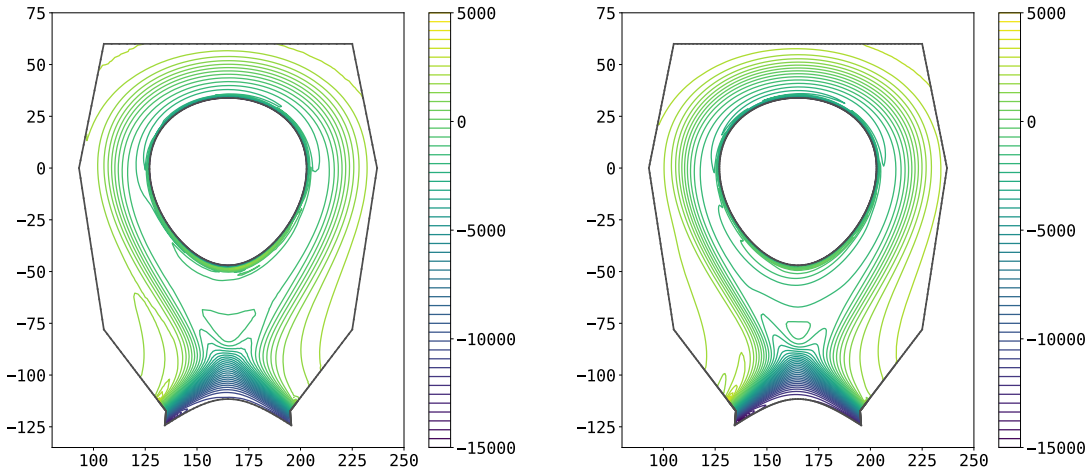

Figure 7: Electrostatic potential $\tilde{\Phi}$ at $t = T$ for the two considered grids: $\dim(V_h) = 34384$, $\dim(Q_h) = 8680$ (left) and $\dim(V_h) = 136864$, $\dim(Q_h) = 34384$ (right).

version shows a much higher convergence rates for the first 100 iterations and is a viable option if an $\mathcal{O}(100)$ reduction of the residual is considered to be satisfactory. For higher accuracy however a more effective strategy would be required.

A detailed investigation of alternative preconditioning strategies is nevertheless outside the scope of the present work, since in order to be useful for the target applications it should also take into account the effects of the terms neglected isolating our model problem (5)–(7) from the complete system (1)–(4). Such an investigation is left for future work.

8 Conclusions

In this paper, we have considered a subset of the equations modeling the SOL layer which captures two key aspects of the complete system: the role of the electrostatic potential as a Lagrange multiplier associated with the quasi-neutrality condition and the geometrical complexity of the system itself. The well-posedness of the reduced problem has been demonstrated and a suitable discretization framework has been proposed, paying attention to avoiding computational solutions that would not generalize to the complete model. The proposed approach has been verified in various numerical experiments. Virtually every aspect of the present work offers room for extensions and improvements: higher order methods can be considered, the error analysis could be refined, possibly taking into account the anisotropy of the problem, more efficient algorithms for the iterative solution of the linear system should be investigated and, most importantly, more terms of the complete model should be included in the analysis. We hope, nevertheless, that the present work can serve as a solid starting point for the development of reliable computational models for the simulation of the SOL layer in fusion devices.

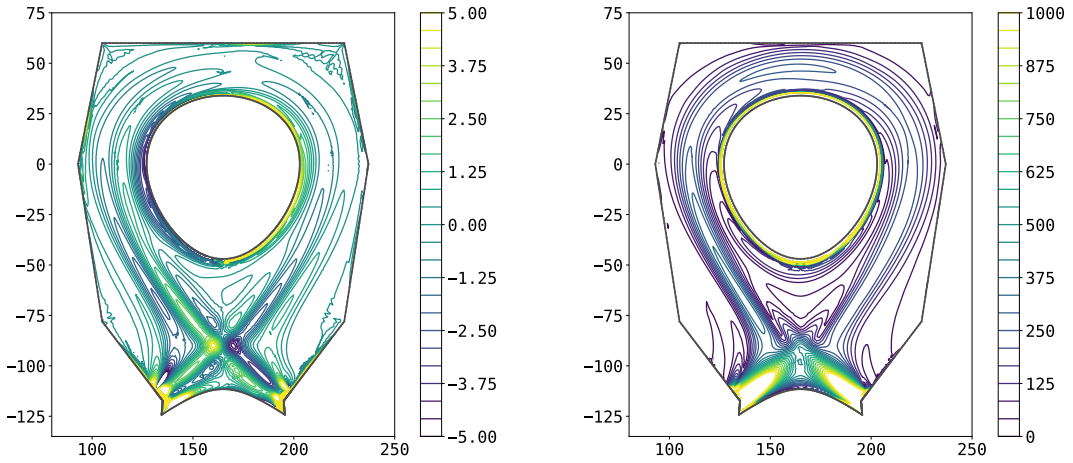

Figure 8: Parallel and perpendicular gradients of the electrostatic potential at $t = T$ for the finest grid with $\dim(V_h) = 136864$, $\dim(Q_h) = 34384$: $(\nabla\Phi)^{\parallel}$, left, and $|(\nabla\Phi)^{\perp}|$, right. Notice that the two figures use different color scales.

Acknowledgments

We kindly thank Bruce Scott and David Coster for many nice and interesting discussions.

This work has been carried out within the framework of the EUROfusion Consortium and has received funding from the Euratom research and training programme 2014-2018 under grant agreement No 633053. The views and opinions expressed herein do not necessarily reflect those of the European Commission.

The work of one of the authors has also been supported by the German Academic Exchange Service.

References

[1] P. C. Stangeby. *The Plasma Boundary of Magnetic Fusion Devices*. Institute of Physics, London, 2000.

[2] S. I. Braginskii. Transport Processes in a Plasma. *Reviews of Plasma Physics*, 1:205, 1965.

[3] W. D. D'haeseleer, W. N. G. Hitchon, J. D. Callen, and J. L. Shohet. *Flux Coordinates and Magnetic Field Structure*. Springer, 1991.

[4] A. Zeiler, J. F. Drake, and B. Rogers. Nonlinear reduced braginskii equations with ion thermal dynamics in toroidal plasma. *Physics of Plasmas*, 4(6):2134–2138, 1997.

[5] B. Scott. The character of transport caused by $e \times b$ drift turbulence. *Physics of Plasmas*, 10(4):963–976, 2003.

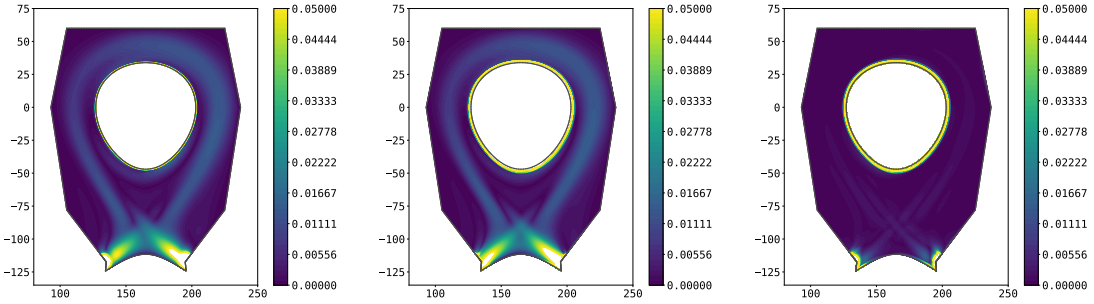

Figure 9: Perpendicular ion and electron velocities at $t = T$ for the finest grid with $\dim(V_h) = 136864$, $\dim(Q_h) = 34384$: $|\tilde{\boldsymbol{u}}^{\perp}|$ (left), $|\tilde{\boldsymbol{u}}_{\mathrm{e}}^{\perp}|$ (center) and $|\tilde{\boldsymbol{u}}^{\perp} - \tilde{\boldsymbol{u}}_{\mathrm{e}}^{\perp}|$ (right).

[6] M. Petravic, G. Kuo-Petravic, and T. Arzt. Fluid models for a tokamak scrape-off plasma. *Contributions to Plasma Physics*, 28(4-5):379–385, 1988.

[7] Dana A. Knoll and Anil K. Prinja. Self-consistent p and e × b drifts in a two-dimensional one-fluid edge plasma model. *Journal of Nuclear Materials*, 176–177:562 – 569, 1990.

[8] T. D. Rognlien, J. L. Milovich, M. E. Rensink, and G. D. Porter. A fully implicit, time dependent 2-d fluid code for modeling tokamak edge plasmas. *Journal of Nuclear Materials*, 196–198:347 – 351, 1992. Plasma-Surface Interactions in Controlled Fusion DevicesProceedings of the Tenth International Conference on Plasma-Surface Interactions in Controlled Fusion Devices.

[9] T. D. Rognlien, J. L. Milovich, M. E. Rensink, and T. B. Kaiser. Simulation of tokamak divertor plasmas including cross-field drifts. *Contributions to Plasma Physics*, 32(3-4):485–490, 1992.

[10] R. Marchand and M. Simard. Finite element modelling of TdeV edge and divertor with $\boldsymbol{E} \times \boldsymbol{B}$ drifts. *Nuclear Fusion*, 37(11):1629, 1997.

[11] V. A. Rozhansky, S. P. Voskoboynikov, E. G. Kaveeva, D. P. Coster, and R. Schneider. Simulation of tokamak edge plasma including self-consistent electric fields. *Nuclear Fusion*, 41(4):387, 2001.

[12] V. Rozhansky, E. Kaveeva, S. Voskoboynikov, D. Coster, X. Bonnin, and R. Schneider. Potentials and currents in the edge tokamak plasma: simplified approach and comparison with two-dimensional modelling. *Nuclear Fusion*, 43(7):614, 2003.

[13] D. Reiter, M. Baelmans, and P. Börner. The EIRENE and B2-EIRENE codes. *Fusion Science and Technology*, 47(2):171–186, 2005.

[14] R. Schneider, X. Bonnin, K. Borrass, D. P. Coster, H. Kastelewicz, D. Reiter, V. A. Rozhansky, and B. J. Braams. Plasma edge physics with B2-Eirene. *Contributions to Plasma Physics*, 46(1-2):3–191, 2006.

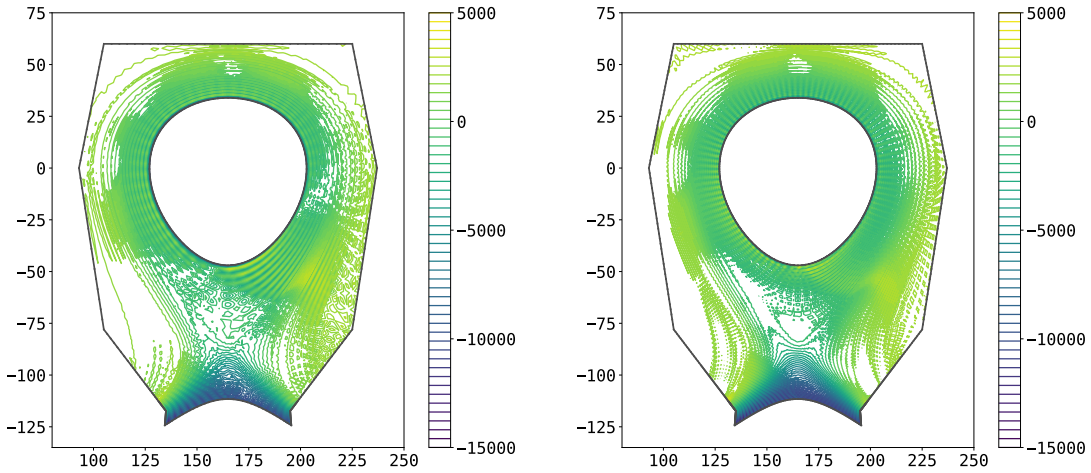

Figure 10: Same as in figure 7 but using the unstable finite element pair $V_h = Q_h$.

[15] J Loizu, P Ricci, F D Halpern, S Jolliet, and A Mosetto. On the electrostatic potential in the scrape-off layer of magnetic confinement devices. *Plasma Physics and Controlled Fusion*, 55(12):124019, 2013.

[16] C. Michoski, D. Meyerson, T. Isaac, and F. Waelbroeck. Discontinuous galerkin methods for plasma physics in the scrape-off layer of tokamaks. *Journal of Computational Physics*, 274:898–919, October 2014.

[17] C. Wersal and P. Ricci. A first-principles self-consistent model of plasma turbulence and kinetic neutral dynamics in the tokamak scrape-off layer. *Nuclear Fusion*, 55(12):123014, 2015.

[18] H. J. Klingshirn, D. P. Coster, and X. Bonnin. Advanced spatial discretizations in the B2.5 plasma fluid code. *Journal of Nuclear Materials*, 438, Supplement:S856–S860, 2013. Proceedings of the 20th International Conference on Plasma-Surface Interactions in Controlled Fusion Devices.

[19] R. Zanino. Finite element fluid modeling of axisymmetric magnetized boundary plasma with recycling neutrals. *Journal of Nuclear Materials*, 196–198:326 – 331, 1992. Plasma-Surface Interactions in Controlled Fusion DevicesProceedings of the Tenth International Conference on Plasma-Surface Interactions in Controlled Fusion Devices.

[20] Th. Pütz, D. Reiter, and M. W. Wuttke. Finite element modelling of the plasma edge. *Contributions to Plasma Physics*, 34(2-3):404–409, 1994.

[21] R. Zanino and F. Subba. Adaptive anisotropic finite elements for edge plasma modeling. *Contributions to Plasma Physics*, 38(1-2):355–360, 1998.

[22] Richard Marchand. Finite element modelling of transport in a tokamak edge and divertor. *Plasma Physics and Controlled Fusion*, 44(6):871, 2002.

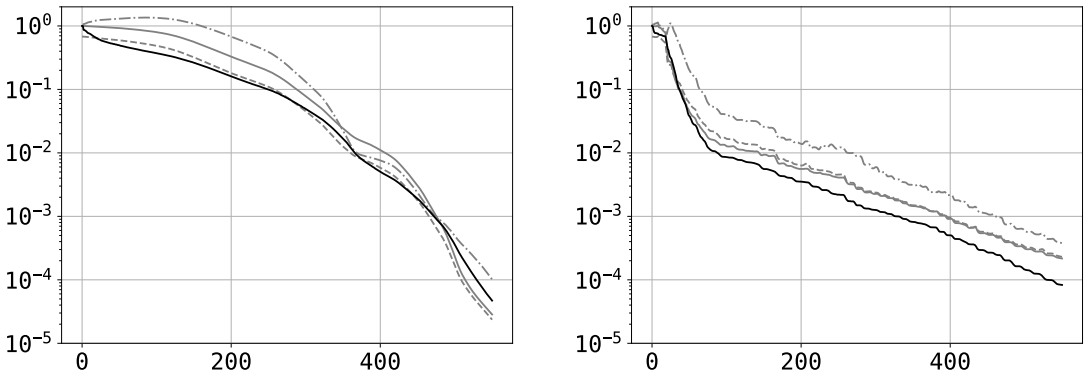

Figure 11: Residual (black solid line) and L^2 error norms for the GMRES iterations advancing the solution from $t_a = 1.25 \cdot 10^{-4}$ to $t_b = 1.875 \cdot 10^{-4}$: $\|\tilde{\boldsymbol{u}}_h - \tilde{\boldsymbol{u}}_h^{(k)}\|_{\boldsymbol{L}^2}$ (gray dashed line), $\|\tilde{\boldsymbol{u}}_{\mathrm{e}\,h} - \tilde{\boldsymbol{u}}_{\mathrm{e}\,h}^{(k)}\|_{\boldsymbol{L}^2}$ (gray dash-dot line) and $\|\tilde{\Phi}_h - \tilde{\Phi}_h^{(k)}\|_{L^2}$ (gray solid line). All the quantities are normalized with the respective value for the initial iteration. Results for the plane GMRES method (left) and for the preconditioned GMRES method (right). Notice that, one the one hand, the residuals are not directly comparable, since they are computed for the plane and the left-preconditioned method, while, on the other hand, the error norms are comparable since they refer to the same quantities and use the same normalization.

[23] F. Subba, A. Airoldi, F. Bombarda, G. Cenacchi, G. Maddaluno, and R. Zanino. Development of a computational tool for limiter edge plasma modeling with application to IGNITOR. *Journal of Nuclear Materials*, 363–365:693–697, 2007. Plasma-Surface Interactions-17.

[24] Fan Zhang, Robert Hager, Seung-Hoe Ku, Choong-Seock Chang, Stephen C. Jardin, Nathaniel M. Ferraro, E. Seegyoung Seol, Eisung Yoon, and Mark S. Shephard. Mesh generation for confined fusion plasma simulation. *Engineering with Computers*, 32(2):285–293, 2016.

[25] F. Subba, X. Bonnin, D. Coster, and R. Zanino. 2D fluid modeling of the ASDEX upgrade scrape-off layer up to the first wall. *Computer Physics Communications*, 179(1–3):194–198, 2008. Special issue based on the Conference on Computational Physics 2007CCP.

[26] M Baelmans, P Börner, W Dekeyser, and D Reiter. Tokamak plasma edge modelling including the main chamber wall. *Nuclear Fusion*, 51(8), 2011. cited By 2.

[27] Giuseppe Alì, Li Chen, Ansgar Jüngel, and Yue-Jun Peng. The zero-electron-mass limit in the hydrodynamic model for plasmas. *Nonlinear Analysis: Theory, Methods & Applications*, 72(12):4415–4427, 2010.

[28] P. Degond, F. Deluzet, and D. Savelief. Numerical approximation of the euler–maxwell model in the quasineutral limit. *Journal of Computational Physics*, 231(4):1917–1946, 2012.

[29] L. C. Evans. *Partial Differential Equations.* American Mathematical Society, 2010.

[30] P. Grisvard. *Elliptic problems in nonsmooth domains.* Pitman, 1985.

[31] R. Temam. *Navier–Stokes Equations.* Elsevier North-Holland, 1977.

[32] A. Quarteroni and A. Valli. *Numerical approximation of partial differential equations.* Springer-Verlag, 2008.

[33] A. Ern and J.L. Guermond. *Theory and practice of finite elements.* Springer-Verlag, 2004.

[34] J. Cahouet and J. P. Chabard. Some fast 3d finite element solvers for the generalized stokes problem. *International Journal for Numerical Methods in Fluids*, 8(8):869–895, 1988.

[35] H. C. Elman and G. H. Golub. Inexact and preconditioned uzawa algorithms for saddle point problems. *SIAM Journal on Numerical Analysis*, 31(6):1645–1661, 1994.

[36] J. H. Bramble, J. E. Pasciak, and A. T. Vassilev. Uzawa type algorithms for nonsymmetric saddle point problems. *Mathematics of Computation*, 69(230):667–689, 2000.

[37] Y. Saad and M. H. Schultz. Gmres: a generalized minimal residual algorithm for solving nonsymmetric linear systems. *SIAM Journal on Scientific and Statistical Computing*, 7(3):856–869, 1986.